The Dissertation Committee for Yaoqing Yang certifies that this is the approved version of the following dissertation:

An Experimental Investigation of Wideband MIMO Channels For Wireless Communications

Committee:

Hao Ling, Supervisor

Guanghan Xu, Supervisor

Edward J. Powers

Qian Niu

Robert W. Heath

Wolfhard Vogel

An Experimental Investigation of Wideband MIMO Channels For Wireless Communications

by

Yaoqing Yang, BS, MSEE

Dissertation

Presented to the Faculty of the Graduate School of

The University of Texas at Austin

in Partial Fulfillment

of the Requirements

for the Degree of

Doctor of Philosophy

The University of Texas at Austin

May 2006

To my wife Yan Xiao, my daughter Yanni Yang, and my family members, with profound love and appreciation.

Acknowledgments

Many people have helped and encouraged me during my Ph.D. research. First of all, I would like to express my deepest appreciation and gratitude to Professor Hao Ling and Dr. Guanghan Xu, my supervisors, for their guidance, encouragement, and help during the course of my graduate research. Combining both great intelligence and an incredible work ethic, Professor Ling showed me how to deal with the scientific problems. I am thankful to Dr. Guanghan Xu, who recruited me into the UT graduate program, for his tremendous help with the implementation of the wideband MIMO channel sounder.

I wish to thank my committee – Professor Edward J. Powers, Professor Robert W. Heath, Professor Qian Niu, and Dr. Wolfhard Vogel – for their generous support and helpful comments during the course of this research, and for their good-natured willingness to adjust their busy schedules. Thanks to Professor Powers, director of the Telecommunications and Signal Processing Research Center, for his suggestions, inspiration, and telecommunication knowledge. I am particularly grateful to Professor Heath, director of the Wireless Systems Innovations Laboratory, for his advice and suggestions on the MIMO channel measurements. Professor Heath's critical comments led to major revisions to my discussion of prototyping. To Professor Niu, I extend my gratitude for his judgment on my research from the point of view of modern physics. I also wish to express my greatest appreciation to Dr. Vogel for his numerous suggestions on experimental setups and thoughtful insights into the measurement results.

During the last three years, I have been working as a teaching assistant for Professor Jeffrey G. Andrews, Professor Baxter F. Womack and Professor Michael F. Becker. I thank them from my heart for their kindness and support as I finished my Ph.D. I also appreciated Professor Mark Carpenter for his expertise on technical writing and his proof-reading this dissertation.

My heartfelt appreciation also goes to my colleagues and friends for their help and encouragement. Thanks to Dr. Jiang Yan, Dr. Adrian Lin, Dr. Anthony J. Ernst, Diane Johnson, Dr. Liang Dong, Matt Starosta, Hang Li, Shobha S. Ram, Xiaoyun Yang, Fanlan Jing, Xiaoqing Yang, Dr. Jian Gu, Dr. Weidong Yang, Dr. Furun Wang, Yanqing Liu, Dr. Jiandong Yin, Xiaoping Hu, and Dr. Yong Zhou.

I am especially indebted to my family members for their love, support, and encouragement during my Ph.D program.

YAOQING YANG

The University of Texas at Austin
May 2006

An Experimental Investigation of Wideband MIMO Channels For Wireless Communications

Publication No. ____________________

Yaoqing Yang, Ph.D.
The University of Texas at Austin, 2006

Supervisors: Hao Ling and Guanghan Xu

Use of multiple antennas in radio links is rapidly becoming the new frontier of wireless communications. In recent years, multiple-input multiple-output (MIMO) systems appear to be promising because they can provide high data rates in environments with rich scattering by exploiting the spatial diversity of antennas. To better understand a real MIMO wireless system and predict its performance under certain environments, it is necessary to develop a wideband MIMO prototype of a wireless channel sounder to examine algorithms and channel models.

This dissertation presents the prototyping of a wideband MIMO channel sounder and the measured channel characteristics of wideband MIMO non-line-of-sight (NLOS) scenarios at a carrier frequency of 1.8 GHz with a bandwidth of 2.5 MHz. The channel sounder, which is a true array system with four transmitting antennas and eight receiving antennas, can accurately capture the wideband MIMO channel features. After the design, implementation, and validation of the wideband MIMO channel sounder, a series of experiments were conducted at the J. J. Pickle Research Campus (PRC), The University of Texas at Austin. Based on the measured data in different environments, the matrix channel impulse responses were extracted. Multipath delay profiles, RMS delay spreads, and the statistics of channel matrices were studied.

Table of Contents

List of Tables

List of Figures

Chapter 1

Introduction

The radio age began in 1897 with the invention of the radiotelegraph by Guglielmo Marconi and since then wireless communication has evolved throughout the world. Progress in radio technology has been creating and improving services at lower costs. Historically, wireless communication expanded slowly, coupled, as it was, to technological improvements. Beginning in the 1980s, however, wireless communication has been growing exponentially along with technology advances in digital signal processing, multiple access schemes, networks, and chip designs.

The first-generation (1G) cellular and cordless telephone networks based on analog frequency modulation (FM) were introduced in 1981. To maximize the capacity in an interference-limited cellular environment, the systems used analog technology and a frequency division multiple access (FDMA) scheme. Examples of the first-generation cellular systems were Advanced Mobile Phone System (AMPS) in North America, Nordic Mobile Telephone System (NMT-450) in Europe, and Nippon Telephone and Telegraph (NTT) in Japan, with channel bandwidths of 30 kHz, 25 kHz, and 25 kHz, respectively [1].

With the advent of very large scale integration (VLSI) chip designs and increasingly sophisticated microprocessor implementation, the second-generation (2G) cellular systems emerged in the 1990s. These systems employed digital modulation techniques and spectrally efficient multiple-access schemes, referred to as time division multiple access (TDMA) and code division multiple access (CDMA). Although these systems were more complex than their analog counterparts, they offered certain benefits, such as increased capacity, the implementation of voice and low data rate (facsimile) services, and enhanced authentication capabilities. Well-known examples of the second-generation systems include the Europe's TDMA Global System for Mobile communication (GSM); North America's TDMA Interim Standard-54 (IS-54), TDMA IS-136, and CDMA IS-95; and Japan's TDMA Personal Digital Cellular (PDC). Moreover, additional services, such as roaming, security, call forwarding, and messaging, were implemented into the 2G systems. Consequently, more spectra in the 1.8 GHz bands were allocated to mobile telephone operations because the growth in usage of these systems was significantly greater than had been predicted. To meet the spectrum requirements, GSM and IS-54 have been up-banded to DCS1800, PCS1900, and IS-154, respectively [1].

With the development of personal communication services (PCS) in recent years, the third-generation (3G) systems are driven by the ever-increasing need for high-speed data transmission with mobile capabilities. The requirements for high data rate, especially packet data transmission, bring new challenges for 3G systems [2]. With substantially enhanced capacity and quality of services, 3G wireless technology can provide users with high-speed wireless access to the Internet and multimedia services anytime, anywhere, and in any form. The 3G system attempts to unify the existing diverse wireless systems into a seamless worldwide radio infrastructure, which will be capable of offering the services of global roaming. A worldwide standard is the Future Public Land Mobile Telephone System (FPLMTS)- renamed as International Mobile Telecommunication 2000 (IMT-2000) in 1995. The 3G standard that has been agreed upon for Europe and Japan is known as the Universal Mobile Telecommunications System (UMTS). UMTS is an upgraded version of the Global System for Mobile Communication (GSM) via the General Packet Radio System (GPRS) or Enhanced Data Rates for GSM Evolution (EDGE). The terrestrial part of UMTS is known as UMTS Terrestrial Radio Access (UTRA). The UTRA standard is a wideband CDMA (WCDMA) technology that features easy integration with the existing GSM protocol. The frequency division duplex (FDD) part of UTRA, which is based on the WCDMA standard, offers very high data rates, up to 2 Mbps. The time division duplex (TDD) part of UTRA is called TD-CDMA. The main global competitor to UMTS standards is CDMA2000, which was developed by Qualcomm in the United States. CDMA2000 can deliver full IMT-2000 capabilities (data rates up to 2 Mbps) in one-third as much spectrum as in WCDMA.

In summary, 3G mobile cellular systems are intended to adopt the diverse wireless systems into a seamless universal standard that will facilitate global roaming and provide a wide range of services, including multimedia. The 3G wireless systems will generally support high-speed voice and data services in many different radio propagation environments, such as 144 kbits/second in vehicular environments, 384 kbits/second in pedestrian environments, and 2.084 Mbits/second in indoor environments.

The expanding range of services provided by wireless communication systems and the explosive increase in the number of subscribers have led to certain challenges, such as limited spectral resource and co-channel interference. Other problems that a wireless system designer has to face include a complex multipath propagation environment, and user demands for higher data rates, better voice quality, longer battery life, and lower infrastructure and operating costs. While a number of different methods, including multiple-access schemes, modulation, and coding, have been used to meet such diverse requirements, the use of multiple antennas at the transmitter and/or receiver in a wireless communication link opens a new dimension of freedom - space, that, if leveraged correctly, can improve performance substantially. For these reasons, many researchers have turned to smart antenna systems that employ antenna arrays coupled with advanced space-time signal processing methods at the base station [3, 4]. By exploiting the spatial dimension in signal processing as a hybrid multiple access technique (space division multiple access, or SDMA), smart antenna systems allow multiple users to transmit co-channel signals, which provides major benefits [5, 6, 7]. For example, beamforming technology focuses the radiation beams of power toward the desired user while steering nulls toward the interferer, thereby significantly improving the signal-to-interference ratio (SIR) which in turn increases the system capacity.

In the recent years, the use of multiple antennas in wireless links at both ends of the transmitter-and-receiver link with appropriate space-time coding/modulation and demodulation/decoding is rapidly becoming the new frontier of wireless communications. Advances in theory include a better understanding of capacity and the performance limits of space-time wireless links, spatial-temporal radio propagation and channel models, and designs for modulation/coding techniques. A growing awareness of the large performance gains of the multiple-input-multiple-output (MIMO) scheme has spurred efforts to integrate this technology into practical systems. In the standards arena, more efforts have gone into introducing spatial multiplexing concepts that require multiple antennas at both ends of the link into the UMTS standard for mobile wireless[8, 9], the IEEE802.16 standard for fixed and nomadic wireless, and the IEEE 802.11 standard for wireless local area networks (LAN) [10].

Therefore, knowledge of the properties of the wireless MIMO channel is necessary for an effective design and performance analysis of multiple antenna systems. For a multiple antenna system, matrix channels denotes the propagation characteristics of the signal present at each antenna element, because a matrix of signal samples is received/transmitted at each instant of time. Matrix channel models are needed to support the development of adaptive array algorithms, cell-site planning, and accurate simulation of MIMO wireless communication systems. The aim of this dissertation is to develop the prototyping of a wideband MIMO channel sounders and measure the realistic radio channels in different outdoor environments.

1.1 Background

To study and model radio propagation characteristics, there is a need to develop the prototyping of a MIMO testbed and conduct measurements in different environments. It is difficult to derive analytically expressions describing how a radio signal propagates through a complex environment. Measurements of the radio channel are usually obtained at the specific site. Moreover, based on realistic assumptions about the nature of the channel, the measured data can be used to construct empirical channel models. Path loss models and wideband multipath models are classic examples of such empirical models. These models are usually site-specific, and they depend on the frequency and type of measurements. In practice, wideband channel measurements are more complicated than narrowband channel measurements. The accuracy of the measurement depends on the channel sounder, the digital signal processing used, the accuracy of the synchronization between transmitter and receiver, and many other factors.

So far, several channel sounding techniques have been used for such purposes. Most employ one of the three following techniques: transmission of a short radio frequency (RF) pulse, use of swept carrier techniques, or a spread spectrum signal with a matched filter receiver. RF pulse systems require large peak power, and pulse amplifiers are expensive. Swept carrier techniques are not suitable for mobile wideband measurements but are quite useful in characterizing the RMS delay spread in indoor scenarios. Usually, a network analyzer is employed for swept carrier wideband measurements. The implementation of spread-spectrum channel sounders is complex, but they provide large coverage areas [11].

Radio propagation models have gradually developed in response to the needs of mobile communication systems as wireless systems have evolved from the 1970s. Much work has been reported in the single-input single-output (SISO) channel modeling area. Early radio propagation models [12, 13] for 1G analog systems accounted only for the large-scale variation of the signal strength and the Doppler characteristics of the radio signal. More specifically, indoor radio channel models were presented in [11, 14, 15, 16], while examples of outdoor channel models can be found in [12, 13, 17]. Propagation models for the 2G digital cellular systems required an expansion to include the temporal properties of the radio channel - power delay profiles, because inter-symbol interference (ISI) caused by multipath dispersion became a limiting factor[18]. Several researchers [1, 19] measured power delay profiles of wireless channels and developed simulation techniques for multipath delay spread in order to determine the circumstances under which equalizers were needed.

With the introduction of multiple antenna systems, spatial information is required in the channel models [20, 21, 22, 23, 24]. Therefore, the single-input multiple output (SIMO) and multiple-input single-output (MISO) channels have also been studied, and different models have been proposed[10, 25, 26, 27, 28]. However, extending these models to the MIMO channel is not straightforward, because the spatial characteristics must then be considered at both ends.

In this work we consider a link for which the transmitter as well as the receiver is equipped with multiple antenna elements. Such a setup is illustrated in Figure 1.1 with M_T transmit antennas and M_R receive antennas. The idea behind MIMO is that the signals on the transmit antennas at one end and the receive antennas at the other end are coupled in such a way that the capacity or data rate (bits/s) of the communication for each MIMO user will be improved. A key feature of MIMO systems is the ability to turn multipath propagation, conventionally a pitfall of wireless transmission, into a benefit for the user. MIMO effectively takes advantage of random fading [20, 21, 22] and, when available, multipath delay spread [23, 24, 25, 26]. The prospect of many orders of improvement in wireless communication performance at no cost of extra spectrum (mainly hardware and complexity are added) has made MIMO a popular topic for new research. This research has prompted progress in areas as diverse as channel modeling, information theory and coding, signal processing, and antenna designs [8, 9, 27, 29, 30, 31].

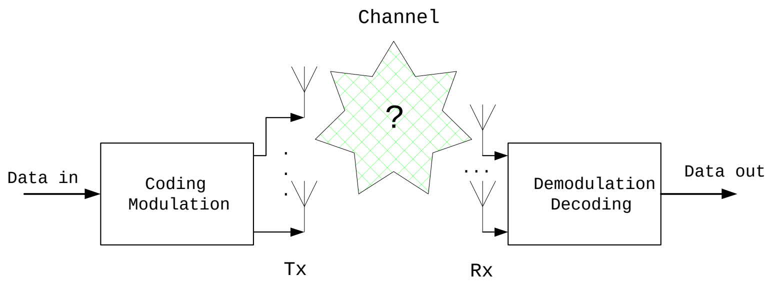

Figure 1.1: Diagram of a MIMO wireless system.

While coding and signal processing are key elements to the successful implementation of a MIMO system [10, 29], the propagation channel and antenna design represent major parameters that ultimately impact system performance. As a result, considerable research has been devoted to the prototyping of MIMO testbed, which can be used to assess the potential of MIMO systems. References [32, 33] provide excellent reviews for the recent MIMO developments.

1.2 Motivation and Objective

1.2.1 Motivation

A wireless communication system based on multiple-input multiple-output technology can achieve high data rates without impacting bandwidth usage, transmitted power, and the range of a system employing conventional technology. Traditionally, wireless-system engineering has used spatial diversity to improve reliability and performance of a wireless communication link, whereas the array-processing community has been interested in target localization. The increasing demand for capacity in wireless systems has motivated considerable research aimed at achieving higher throughput on a given bandwidth. One important finding of this activity is that, for an environment sufficiently rich in multipath components, the wireless channel capacity can be increased using multiple antennas on both the transmit and receive sides of the link [20, 23, 34]. For example, recent research results have demonstrated data rates as high as 40 bits/s/Hz in an indoor environment [21, 35]. The multipath structure has been exploited for space-time coding algorithms. Therefore, in order to assess the performance of systems that implement these algorithms, it is important to gain a full understanding of the complex spatial behavior of wireless multiple-input multiple-output channels.

Past methods for characterizing multipath MIMO channels included approximate statistical analyses and ray-tracing procedures [36]. Those solutions offered information concerning general channel behavior but suffered from their inability to accommodate an adequately detailed representation of the propagation environment [37]. More recently, experimental measurement campaigns have been initiated to statistically characterize both indoor and outdoor wireless MIMO channels [22, 38, 39, 40]. Results from those experiments have provided considerable insight concerning the capacity increases from the possible use of MIMO systems. Rapid prototyping of a MIMO testbed provides a new way to verify the state-of-the-art MIMO algorithms. With a greater understanding of signal propagation in different environments and with improved matrix channel models, system engineers can effectively use multiple antennas to design spectrally efficient, high-capacity, high-quality wireless communication systems.

1.2.2 Objective

The main objective of this dissertation is to develop the prototyping of a wideband MIMO testbed and investigate the wideband MIMO channel characteristics based on a series of outdoor channel measurements. Therefore, this dissertation contributes to our knowledge of the wideband MIMO channel sounder:

- The primary objective is to develop a prototype of a wideband MIMO channel sounder. Therefore, a prototype of a state-of-the-art wideband MIMO channel sounder is designed and implemented with spread spectrum technology. The operating frequency is 1.8 GHz and bandwidth of 2.5 MHz.

- The second objective is to validate and measure the outdoor radio channels. Detailed calibration procedures are described and the features of measured wideband channels, such as the RMS delay spreads and frequency correlation functions, are presented.

1.3 Organization of the Dissertation

This dissertation is organized as follows. Chapter 2 introduces the radio environments and covers the review of the prototyping of MIMO channel sounder. Chapter 3 provides a detailed description of the wideband MIMO channel sounder that has been developed at The University of Texas at Austin. Chapter 4 describes the measurement environments and wideband channel measurements. Chapter 5 presents the MIMO channel capacity, which covers the basics of channel capacity, the measured MIMO channel capacity, and evaluation of the Kronecker MIMO channel model. Finally, Chapter 6 summarizes the dissertation and provides suggestions for future research.

1.4 Nomenclature

AMPS	:	Advanced Mobile Phone System
AWGN	:	Additive White Gaussian Noise
BLAST	:	Bell Labs layered space-time
BS	:	Base Station
CCDF	:	Complementary Cumulative Density Function
CDF	:	Cumulative Density Function
CDMA	:	Code Division Multiple Access
DECT	:	Digital European Cordless Telephone
DOA	:	Direction of Arrival
EERL	:	Electrical Engineering Research Laboratory
EVD	:	Eigenvalue Decomposition
FDD	:	Frequency Division Duplex
FDMA	:	Frequency Division Multiple Access
FPGA	:	Field Programmable Gate Array
GPS	:	Global Positioning System
GSM	:	Global System Mobile
GWSSUS	:	Gaussian Wide Sense Stationary Uncorrelated Scattering
IF	:	Intermediate Frequency
iid	:	Independent Identically Distributed
IMTS	:	Improved Mobile Telephone Service
IS-54/95/136	:	Interim Standard-54/95/136

ISI	:	Inter Symbol Interference
LOS	:	Line-of-Sight
LMS	:	Least Mean Squares
MAI	:	Multiple Access Interference
MIMO	:	Multiple-Input Multiple-Output
MISO	:	Multiple-Input Single-Output
MSE	:	Mean Squared Error
MSV	:	Modified Saleh-Valenzula's Model
MT	:	Mobile Terminal
MUSIC	:	MUltiple SIgnal Classification
NLOS	:	Non-Line-of-Sight
NMT	:	Nordic Mobile Telephone
OFDM	:	Orthogonal Frequency Division Multiplexing
PCS	:	Personal Communications Services
PDC	:	Personal Digital Cellular
PDF	:	Probability Distribution Function
PN	:	Pseudo-random Noise
RF	:	Radio Frequency
RMS	:	Root Mean Square
Rx	:	Receiver
SAS	:	Smart Antenna System
SDMA	:	Space Division Multiple Access

SIMO : Single-Input Multiple-Output

SISO : Single-Input Single-Output

SIR : Signal-to-Interference Ratio

SNR : Signal-to-Noise Ratio

SS : spatial signature

SVD : Singular Value Decomposition

TDD : Time Division Duplex

TDMA : Time Division Multiple Access

TOA : Time of Arrival

Tx : Transmitter

UCA : Uniform Circular Array

ULA : Uniform Linear Array

VCIR : Vector Channel Impulse Response

WLAN : Wireless Local Area Networks

Chapter 2

Radio Propagation and Prototyping Testbed

In wireless communication, the electromagnetic waves travel along different paths of varying lengths. Each path involves reflection, diffraction, and scattering caused by buildings, terrain structures, and various man-made objects between the transmitter and the receiver. Thus, the received signal is a combination of delayed and attenuated replicas of the transmitted signal with distortions. This kind of distortion is called *fading*. Unlike wireline channels, wireless channels change dramatically due to the environment and show a time-variant nature due to motions.

Figure 2.1 illustrates a typical wireless propagation environment where the base station (BS) antenna is higher than the surrounding objects. Far from the BS, a mobile terminal (MT) travels within the surrounding objects. In such environments, the radio wave propagation is basically characterized by two types of fading: *large-scale fading* and *small-scale fading*.

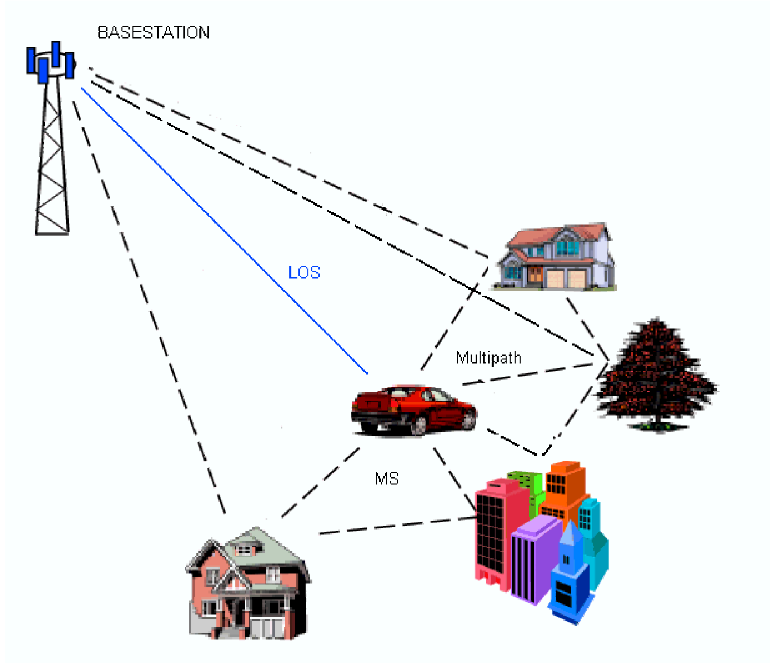

Figure 2.1: Illustration of the mobile radio channel

2.1 Classification of Fading Channels

A radio signal transmitted into a wireless channel is dispersed in two ways: in the time-domain dispersion is caused by multipath delay spread τ_{rms}, and in the frequency-domain dispersion is caused by Doppler spread f_d. Thus, wireless channels are time-dispersive and/or frequency-dispersive. Based upon the transmitted signal period T_s, the channel coherence time T_c, the transmitted signal bandwidth B_s, and the channel bandwidth B_c, the channels can be classified into four groups: time-flat, frequency-flat, flat-flat, and non-flat [1]. The channel is considered to be time-flat when it remains constant during at least the transmission time of one symbol. In other words, the channel is time invariant. By analogy, the channel is referred to as frequency-flat when the bandwidth of the transmitted signal is smaller than the coherence bandwidth of the channel. This means that the channel is frequency nonselective or narrowband channel. When the channel is flat in both time and frequency, it is called a flat-flat channel. In such a case, the transmitted signal bandwidth undergoes the same attenuation at each frequency, and the channel remains unchanged during the transmission of one symbol. Last, a channel is called non-flat when it is both time variant and frequency selective. Details of the classification of channels are shown in Figure 2.2.

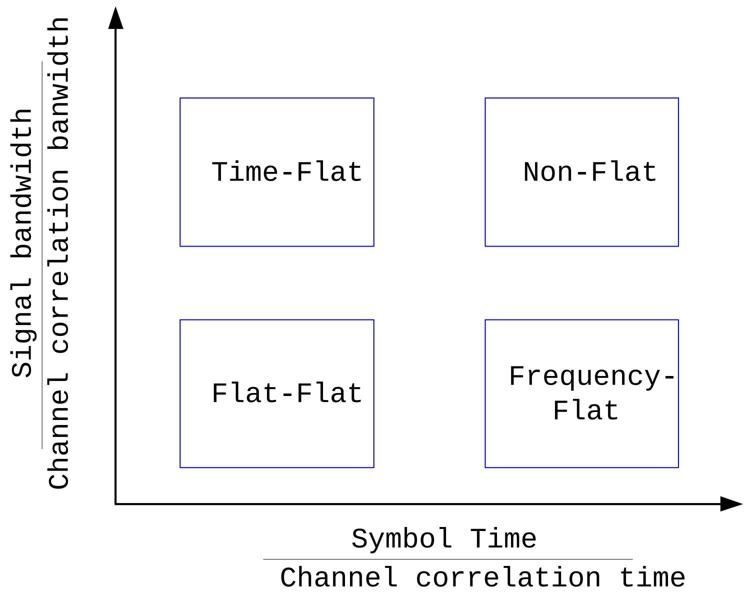

Figure 2.2: Classification of fading channels.

2.2 MIMO Channel Model

Theoretically, the matrix channel is an extension of the vector channel. Consider a wireless communication system with M_T transmitting antennas and M_R receiving antennas, as shown in Figure 2.3. This arrangement of multiple antennas at both the transmitter and receiver forms a typical matrix channel. In practice, the MIMO channel models can be classified in different ways based

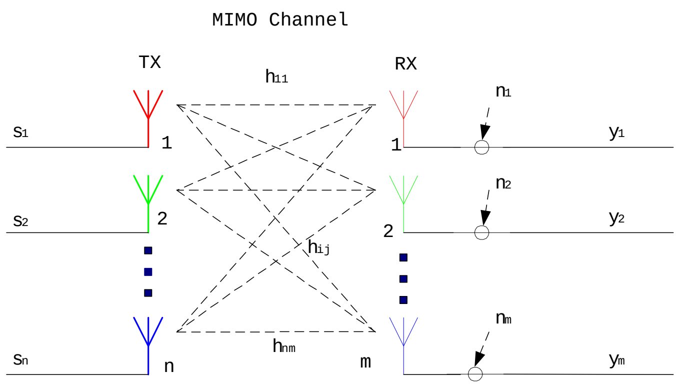

Figure 2.3: MIMO channel model

on both the channel features and the applications [11, 41].

2.2.1 Narrowband vs. Wideband

A radio channel is called a narrowband channel if the channel coherent bandwidth is larger than the baseband signal. It is also called a flat-flat channel, because each transmitted frequency component undergoes the same fading. The frequency structure does not change. When the channel coherent bandwidth is less than the baseband signal, the radio channel is called a wideband channel. It is sometimes called a frequency-selective fading channel, because each transmitted frequency component undergoes different fading. The channel medium is very dispersive in a frequency-selective fading channel. The received signal contains a delayed, distorted, and attenuated version of the transmitted signal, and this produces intersymbol interference (ISI), which usually degrades communication performance.

Similarly, the MIMO channel models can be divided into wideband models and narrowband models directly by considering the bandwidth of the system. The wideband models treat the propagation channel as frequency selective, which means that different frequency sub-bands have different channel responses. In contrast, the narrowband models assume that the channel is flat-fading and therefore the channel has the same response over the entire system bandwidth.

2.2.2 Physical vs. Non-Physical Models

The MIMO channel models can also be divided into physical and non-physical models. The physical models generally choose some crucial physical parameters to describe the MIMO propagation channels. The typical parameters include angle of arrival (AOA), angle of departure (AOD), and time of arrival (TOA). However, under many propagation conditions, the MIMO channels are not well described by a small set of physical parameters, and this limitation makes it difficult to identify and validate the models. Another category is non-physical models, which are based on the channel statistical characteristics. In general, the non-physical models are easy to simulate and provide accurate channel characterization for the situations under which they were identified. These models, however, give limited insight into the propagation characteristics of the MIMO channels. Specifically, those limitations are set by the channel sounder characteristics, such as, the bandwidth, configuration, and aperture of the arrays, and the heights of the transmit and receive antennas in the measurements.

2.2.3 Measurement-Based vs. Scattering Models

To model a MIMO channel, one approach is to measure the real MIMO channel responses through field measurements. Some important characteristics of the MIMO channel can be extracted from recorded data, and the MIMO channel can be modeled to have similar statistical characteristics. An alternative approach is to postulate a model (usually involving distributed scatterers) that attempts to capture the channel characteristics. Such a model can often illustrate the essential characteristics of the MIMO channel as long as the constructed scattering environment is acceptable.

2.3 Prototyping Testbed

The assessment of proposed space-time coding techniques relies on accurate channel models, detailed channel measurements, and prototyping testbeds. Channel modeling is attractive since simulations may be executed quickly on a computer, and results are reproducible at minimum costs. Detailed channel measurements go one step beyond channel modeling, allowing the space-time coding designer to test proposed algorithms on real-world channels. Unfortunately, detailed measurements are somewhat scarce, and those that are available represent only a small fraction of possible propagation channels. Thus, it is absolutely necessary to conduct MIMO channel measurements in various environments. Prototyping reduces risk when communication systems based on new technology are to be developed. Prototyping allows for fixed-point solutions and design space exploration and for the comparison of various hardware architectures. A special design flow offers rapid prototyping of various DSP and FPGA structures allowing few people to convert algorithmic design ideas into real-time experiments. There are many different kinds of MIMO testbeds. Following are brief reviews of some typical MIMO testbeds.

2.3.1 Narrowband MIMO Channel Sounders

1. In [42], a narrowband MIMO channel sounder was built to measure the complex channel coefficients in outdoor environments between a 16-element transmit array and a 16-element receive array. The transmitter array radiated a unique continuous wave (CW) tone from each of its antennas. The tones were separated by 2 kHz, thus occupying 32 kHz. Each transmitter was labeled by a different CW transmitted frequency. These frequencies were 2.11 GHz + (0, 2, 4, $\cdots$, 30 kHZ). All these frequencies were simultaneously received by the 16 receivers, and then, down-converted, digitized, and Fourier transformed. The results were the transfer coefficients between every possible combination of receive-transmit antenna pairs. These coefficients were arranged in a 16 x 16 transfer matrix. This bandwidth was regarded as narrow, such that any differences between the antennas were due to spatial displacements of the antennas and not to frequency selective effects. The receiver consisted of 16 identical radio chains and a digitizer, which can simultaneously sample all receivers. To identify the tones at the receiver, the fast Fourier transform (FFT) was used during post processing. Both transmitter and receiver were frequency locked to GPS. Transmit power was 23 dBm per element.

2. In [37], the experimental platform uses a custom MIMO communications

system operating at 2.45 GHz to directly measure the wireless MIMO channel transfer matrix. The transmitter generates N unique binary codes using a digital pattern generator and mixes them with a local oscillator to produce N distinct co-channel binary phase shift keyed (BPSK) signals. The resulting signals are amplified to 27dBm and fed into one of the N transmit antennas. The receiver amplifies and downconverts the signals from each of the M antennas. The resulting M intermediate frequency (IF) signals are low-pass filtered, amplified, and sampled using a 16-channel 1.25 Msample/s card for storage on the PC.

The transmit system consists of a custom radio frequency (RF) subsystem that accepts binary sequences from an external digital pattern generator and a local oscillator (LO) signal from a tunable microwave source. The subsystem distributes these signals to 16 individual cards, each of which amplifies the LO signal and multiplies it with one of the binary sequences to produce BPSK modulation. The resulting signal is amplified to 0.5 W and fed to one of the transmit antennas. The pseudo random binary sequences used in the system are constructed using a shift-generator initialized with a maximum-length sequence polynomial.

The receive system consists of a second RF subsystem that accepts a LO signal from a microwave source. Each of 16 receive cards amplifies, downconverts, and filters the signal from one of the receive antennas. The resulting intermediate frequency (IF) signals are sampled on a 16-channel 1.25 Msample/s analog-to-digital (A/D) conversion card for storage on the PC. This data is then postprocessed. This processing first involves symbol timing recovery and carrier recovery stages to obtain synchronous complex baseband signals. A Maximum Likelihood algorithm is then used to estimate the channel matrix. For this study, the use of 1000- bit binary codes at a chip rate of 12.5 kbps yielded a nominal bandwidth of 25kHz.

3. In [28], MIMO measurements are set up by a 4 x 4 system. The Tx uses a 1-to-4 switch with a switch time of $50\mu s$ between each element of the antenna array, implementing a pseudo parallel transmission. The BS consists of eight parallel Rx channels; nevertheless, due to the configuration setup, only four channels will be considered. Channel sounding measurements were performed every 20 ms at a carrier frequency of 2.05 GHz and a chip rate of 4.096 Mcps. The complex narrowband information has been extracted from the wideband channel data by averaging the complex delayed signal components. MS and BS were connected by 10 m coaxial cables. The height of the antenna arrays at the MS and the BS were 1.69 m and 2.34 m, respectively. The measurements were made free from people moving around the antennas to investigate time stationary picocell environments. The MS was moved along the slide over a distance of 9λ.

2.3.2 Wideband Virtual Array MIMO Channel Sounder

1. In [43], the measurement equipment was a Medav RUSK BRI vector sounder, which has an 8-element omnidirectional uniform linear array (ULA) at the transmitter side and an 8-element ULA with 120° beamwidth at the receiver side. The measurement setup was centered at 5.2 GHz. The distance between two neighboring antenna elements was 0.5λ for

both arrays. There was a feedback from the receiver to the transmitter by a cable maintaining the coherence between the transmitter and receiver. A periodic multifrequency signal with 120 MHz bandwidth was sent out by the transmitter and captured by the receiver. The channel response was then estimated and saved in the frequency domain. The maximum expected channel excess delay was $0.8\mu s$, corresponding to 97 frequency subchannels. For each transmit element, one vector snapshot (one measurement from each receive element) was taken by the receiver through switching control circuits. The sampling time for each full MIMO snapshot (8 vector snapshots) was $102.4\mu s$, which is well within the coherence time of this indoor environment. One complete measurement included 199 blocks with 16 MIMO snapshots within each block; therefore, there were 199 x 16 = 3184 complete MIMO snapshots in total for each frequency subchannel. The time delay between two neighboring blocks was 26.624 ms. This means the total time for one complete measurement was 5.3 s.

2. In [24], the measurement device was a RUSK ATM channel sounder with a bandwidth of 120 MHz, connected via a fast RF switch to a uniform linear receiver antenna array. This array consisted of 8 antenna elements ($\pm 60^\circ$ element-beamwidth), plus two dummy elements at each end of the array. It consisted of a monopole antenna mounted on a X-Y positioning device with stepping motors. The positioning was controlled by a personal computer (PC) via a serial RS 232 interface.

   The raw data were acquired using a two-sided multiplexing technique. At the receiver, the RF switch was connected to the first antenna element of the array, so that the transfer function (measured at 192 frequency samples) from the first transmit to the first receive element of array was sounded. Then, the switch was connected to the next receive antenna element, and the next transfer function was measured. The measurement of all those transfer functions was repeated 256 times in order to assess the time variance of the channel. Then, the transmit antenna was moved to the next position, and the procedure was repeated. The regularly sampled data (in frequency, time and two spatial domains) were buffered onto a harddisk of a computer.

For a correct extraction of the multipath parameters, transmitter and receiver must be properly synchronized in time and frequency. This was achieved by connecting transmitter (TX) and receiver (RX) by an optical fiber. The effect of signal runtime through the fiber and the signal processing delays were eliminated by back-to-back calibration. Any virtual array requires that the channel remains static during the measurement period. In this case, one complete measurement run (2 x 8 antenna positions at TX x 8 spatial samples at RX x 192 frequency samples and 256 temporal samples give 16 x 8 x 192 x 256= 6,291,456 complex samples) took about 5 minutes.

There are some advantages of the virtual array-technique: 1) it is more versatile than the physical- array arrangement; and 2) there is no mutual coupling to neighboring elements, so that no calibration is required.

2.3.3 MIMO-OFDM Channel Sounder

1. The Motorola system in [44]: This broadband communication system was developed for implementing and evaluating these candidate physical-layer technologies. The data collected by this experimental system can also be used to characterize the MIMO impulse response characteristics in a 20 MHz bandwidth at 3.7 GHz with two transmit and two receive antennas.

   The construction of the 20 MHz channel bandwidth OFDM signal is as follows. It consists of 751 subcarriers spaced 25 kHz apart, resulting in a signal bandwidth of 18.775 MHz. Nulls are placed at each of the spectra to provide a guide band for DAC and filtering. A 1024-point IFFT transforms this frequency domain data into time domain, and the resulting time-domain signal is sampled at 25.6 MHz. A 25% cyclic extension (256 samples) is split into a prefix and a postfix and added to the time-domain signal to combat multipath and inter-symbol interference. The transmitter uses a programmable arbitrary waveform generator as a source to continuously transmit two independent OFDM test signals that are amplified up to 45 dBm. At receiver, the received RF signals are downconverted to 38.4 MHz IF signals and sampled at 51.2 MHz with 12 bits of resolution. The transmitter and receiver are each locked to GPS-derived 10MHz references, thereby eliminating frequency offset between the two timebases.

2. The Stanford system in [45, 46]: A custom measurement system was designed and implemented in hardware, which allowed the measurement of the complex channel response of a 2 x 2 MIMO channel at 2.48 GHz

center frequency. The system was based on swept frequency sounding. A narrowband test signal was swept in 200 kHz steps across a 4 MHz frequency band every 84 ms. The narrowband receiver was swept synchronously with the transmitter, with timing references derived from rubidium clocks. The advantage of this design is a low-noise floor (narrow bandwidth) and reduced complexity compared to spread-spectrum systems. The recorded channel response data was streamed to computer harddisk for later processing.

3. The UT system in [47]: This 2 x 2 MIMO-OFDM implementation operates at 2.4 GHz with a bandwidth of 16 MHz. OFDM with 64 tones is employed over all bandwidth. The length of the cyclic prefix is 16 samples. This corresponds to an OFDM symbol duration of $5\mu s$, with a guard interval of $1\mu s$ and a data portion of $4\mu s$. OFDM symbols in 200 ms data packets are transmitted. This 200 ms was determined by memory sizes at the receiver, which prevented longer acquisition periods. National Instruments RF hardware was the core of the prototype. Each pair of transmitters and receivers was housed in separate PXI chassis. Each PXI chassis was connected to a PC through a PCI bridge that connects the PXI hardware to the PCI bus. At the transmitter, a RF signal generator uses the arbitrary waveform generator (AWG). The AWG acts as the digital-to-analog converter (DAC), and it operates at a maximum of 100M samples/s with a 16-bit resolution. The AGW has a 256MB buffer. When transmitting complex data, the AGW itself upconverts the signal to an intermediate frequency of 25 MHz before the signal is sent to the RF upconverter. The upconverter can move a signal spec-

trum up to a carrier frequency of 2.7 GHz with bandwidths up to 20 MHz and is capable of a maximum of 13 dBm of output power. The AGW has a trigger line available for timing synchronization, while the up-converter has an input available for clock synchronization.

The receiver consists of two units: an RF down-converter and a digitizer. The down-converter can transpose the RF signals into an IF frequency of 15 MHz before sending to the ADC. The digitizer runs at a maximum sampling rate of 64 Msamples/s with a 14-bit resolution. It is equipped with a 64 MB buffer. The digitizer samples the IF waveform and sends it to the PC, where IF demodulation happens in software. This software demodulation, along with the limited speed of the PCI bus, prevents continuous operation at maximum bandwidth. To extend the usable range of the prototype, a low-noise amplifier Mini-circuits ZQL-2700MLNW was used at the receiver. Additionally, for timing and clock synchronization, a three-way power splitter was used to send each signal out to each of the transmit and receive components. So the system is good enough to conduct indoor short-range measurements.

2.4 Summary

Prototyping of a MIMO channel sounder provides an easy way to study the radio channels and algorithms. In Chapter 2, we introduce the matrix channel models and the prototyping of MIMO channel sounder. Such models are necessary in order to analyze the statistical properties of the measured data. Before looking into the measured channel characteristics, we will first present the prototyping of a wideband MIMO channel sounder in the next chapter.

Chapter 3

Design and Implementation of Wideband MIMO Channel Sounder

3.1 Introduction

There are many techniques to measure a radio channel. The choice of a particular technique depends on the set of desired channel parameters and radio environments. In narrowband measurements, the measured results do not provide information on the time delay of any individual path. Rather, they reflect the vector addition of the complex amplitudes of the arriving paths as observed in the power fluctuations in the received signal [1]. Wideband measurements, in contrast, provide information on the multipath delay spread and the structure of individual paths, as well as the frequency selectivity of the channel. Therefore, wideband channel measurements resemble the measurement of the impulse response or overall frequency response of interest [11]. The technique of wideband channel measurement can be categorized with respect to the domain in which the measurements are performed.

- *Time-domain sounding*: Pulse sounding is the most commonly used technique in radio channel measurements. This method is based on the transmission of a single pulse. The signal detected at the receiver consists of a train of pulses due to multipath effects. From the received signal, the channel power delay profile (PDP) is estimated, but no phase information is available. In practice, there is a power limitation at the transmitter, so that the path distances of measurement are typically no greater than 100 m. The time resolution of the measurements is inversely proportional to the bandwidth of the measurement system. However, the method is fast and well suited for determining the power delay profile.

- *Frequency-domain sounding*: This technique uses a network analyzer to sweep the bandwidth with a carrier of interest. As a result, the channel transfer function is obtained. This technique implies coherent measurements, and information on both the magnitude and phase is acquired. With the complex transfer function in the frequency domain, a transformation to the time domain is possible by inverse fast Fourier transform (IFFT). The advantage of this method over the time-domain measurements is that the accuracy of the time-domain representation is limited only by the frequency range of the sweep. The disadvantage of this method is that the channel has to remain unchanged during the operation. Consequently, no Doppler effects can be measured. Another disadvantage is that the phase reference is required at the receiver site.

Therefore, the reference phase is usually supplied by a cable from the transmitter, which limits the distance between the transmitter and the receiver. Recently, it was reported that the Tx and Rx are each locked to a GPS-derived 10 MHz reference, thereby eliminating frequency offsets between the two timebases [44, 48].

- *Correlation sounding*: This technique employs the correlation properties of the spread spectrum. Correlation is widely used to compare the similarity of two complicated things. For example, if two signals in time domain are totally different, their correlation tends to zero. In contrast, if two signals look almost the same, then their correlation is close to 1. By this method, a local oscillator signal is modulated with a pseudo-random sequence and transmitted over a channel. At the receiver, the same pseudo-random sequence is used to retrieve the transmitted signal. In practice, the sequence generator at the receiver runs at a slightly slower speed than that at the transmitter. As a result, different multipath components are sequentially correlated with the code. The method is often used to perform measurements in frequency bands that are occupied by the existing communication systems [11, 49]. In this work, the correlation sounding technique is selected to implement the wideband MIMO channel sounder. The channel coefficients are estimated off-line during data processing.

3.2 Principles of Wideband MIMO Channel Sounders

In this section, the principle of the wideband channel sounder is described in detail. First, let us consider a complex pseudo-random noise (PN) sequence $\mathbf{s}(n)$, $\{n = 1,\ 2,\ \cdots,\ K\}$ with $K = 120$ data points, which is called the base PN probing sequence. The length of $\mathbf{s}(n)$ is decided by the hardware in the system. The real part and the imaginary part are shown as Figure 3.1. Next,

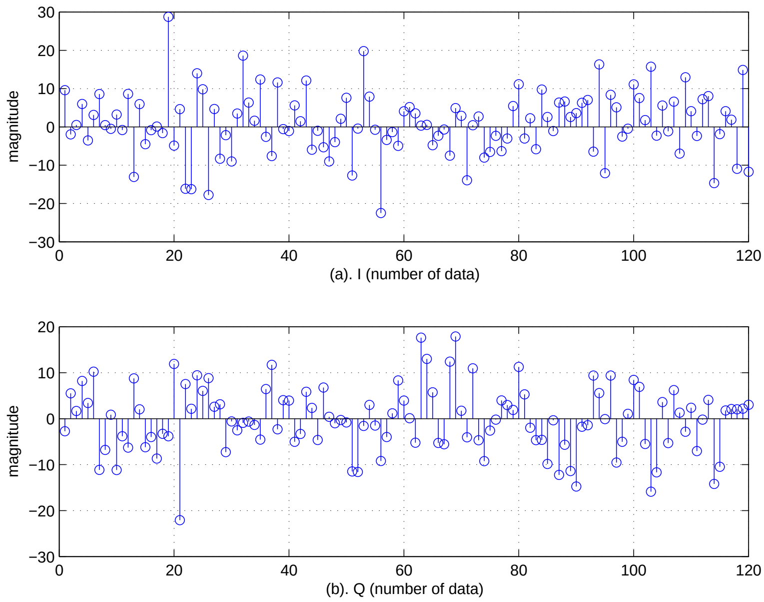

Figure 3.1: The base pseudo-random noise signal.

we develop four transmitted signals from the base PN probing sequence by circularly shifting one quarter length of data points(which is 30 in this system). This process is demonstrated in Figure 3.2. Thus, the in-phase (I) and quadrature (Q) branches of all four Tx sequences: $[\mathbf{s}_1(n),\ \mathbf{s}_2(n),\ \mathbf{s}_3(n), and\ \mathbf{s}_4(n)]$ are composed of 120 data points, respectively. Thirdly, the prefix and postfix are

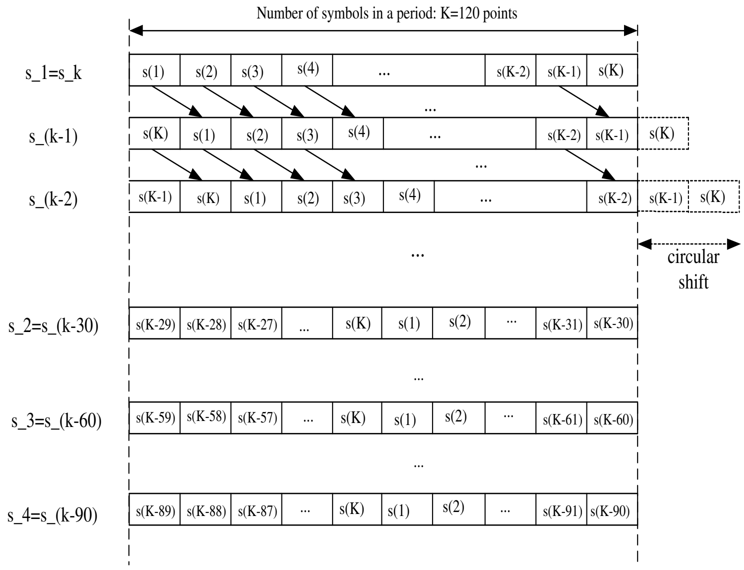

Figure 3.2: Generation of four Tx signals.

added to each of the Tx probing sequences so as to synchronize easily during post data processing. We extract the last 30 data points as the prefix, and move the first 30 data points as the postfix. Consequently, we get four Tx PN sequences with 180 data points, depicted as in Figure 3.3. The last process is to oversample those data points by four-times , and then to convolve them with a raised-cosine pulse-shaping filter of 33 data points. The final length of sequence is 752 data points. In our wideband MIMO testbed, the chip rate is designed to be 10 MHz. In other words, the sampling rate of both ADC and DAC for the baseband signal is 10 MHz. The spectrum of the Tx1 signal is shown in Figure 3.4. As we can see, the bandwidth of the probing signal is around 2.5 MHz. Also note that there are negative frequency components in the probing signal due to its composition of an in-phase and quadrature branch.

To validate the system performance, simulation has been done in ad-

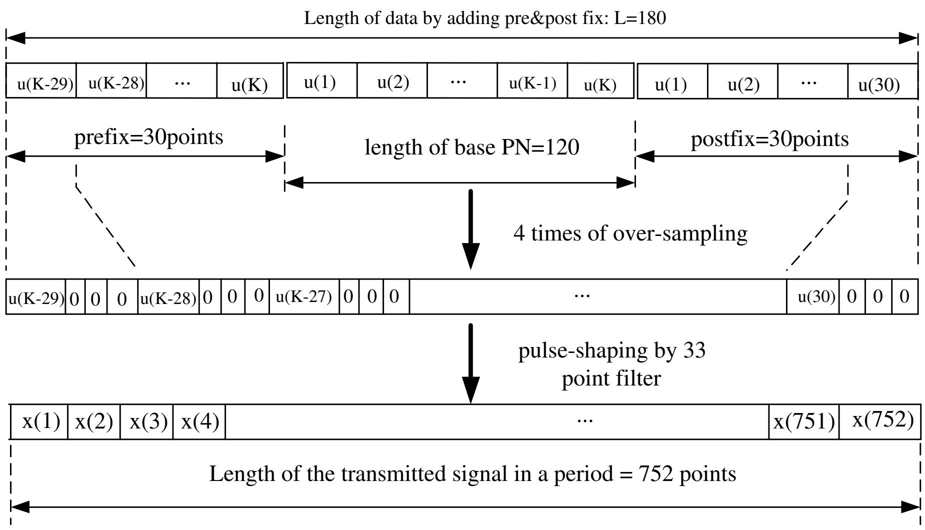

Figure 3.3: Pre-process of Tx data.

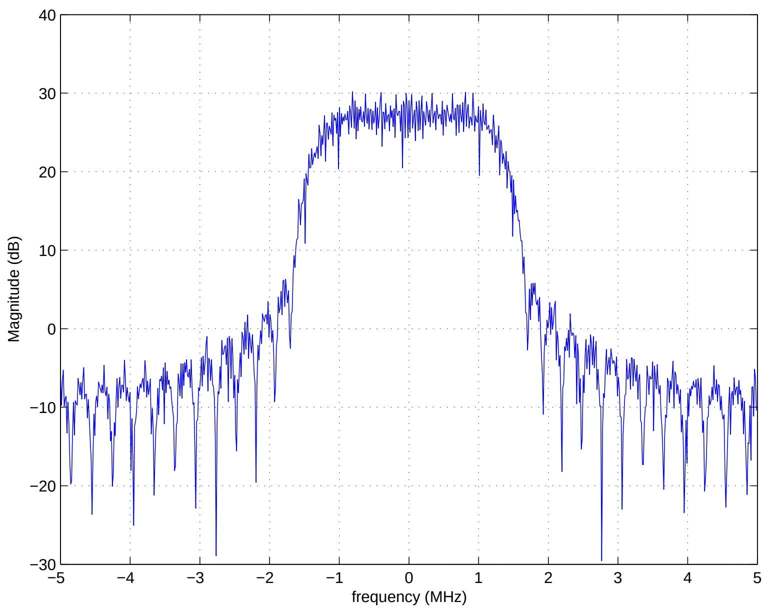

,

Figure 3.4: Spectrum of Tx signal

vance. If we assume that one of the four Tx is launched, only one Rx is put to work, the Tx and Rx are synchronized perfectly, and the four channel coefficients are set to 1, the received signal should be $r(n) = s_i(n); (i = 1, 2, 3, 4)$ (after four-time down-sampling and removing the cyclic prefix and postfix). The cross-correlation results of $r(n)$ with the base PN probing sequence $s(n)$ in one period of time are shown in Figure 3.5. As we can see four peaks appear at different time-delay instances.

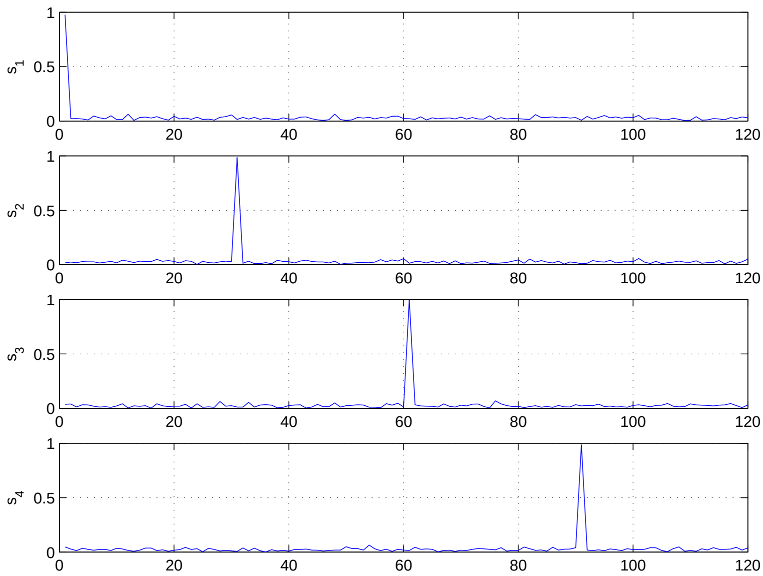

Figure 3.5: Cross-correlation of received signal, assuming $h_{1,1:4} = 1$

Next, consider a multipath channel with four transmitters and one receiver. If we assume a channel with a LOS and an echo of $1.2\mu s$ delay relative to the LOS signal's arrival time, and four echoes with four different reflection coefficients, the cross-correlation results between the received signals and base PN probing signal are shown in Figure 3.6, assuming the chip rate of 10 MHz. Because the four Tx transmit continuously, the cross-correlation between the received signals and base probing signal is accomplished in the frequency do-

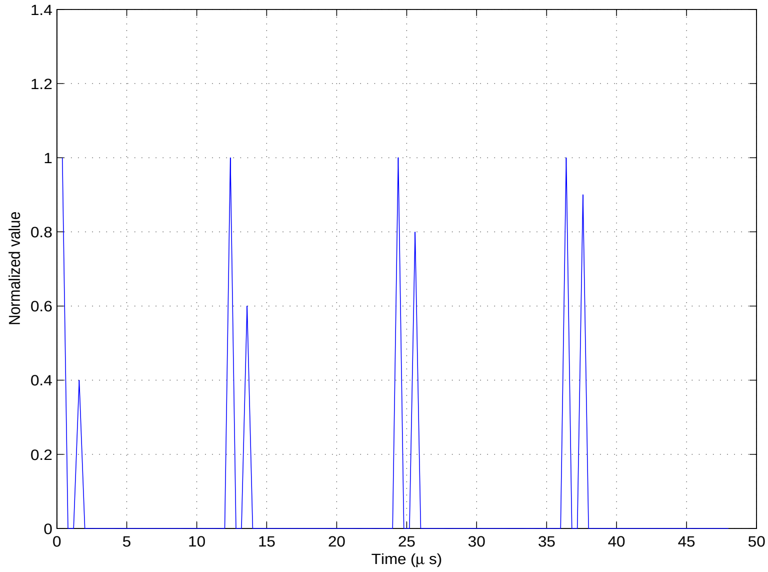

Figure 3.6: Cross-correlation of the received signal with base PN sequence

main by a Fast Fourier Transform (FFT) due to the cyclic convolution property of the Tx sequences. We observe that the maximum delay is 12μs for each link between the Tx and Rx. In other words, the channel sounder is capable of detecting a delay less than 12μs.

3.3 Hardware of Wideband MIMO Channel Sounder

3.3.1 Transmitter

The Tx testbed consists of four identical transmitting modules, a local oscillator (LO) synthesizer board, four dual-channel digital-to-analog converters (DAC), and a field-programmable gate array (FPGA) board. The block diagram is shown as Figure 3.7. Each Tx module transmits a probing signal

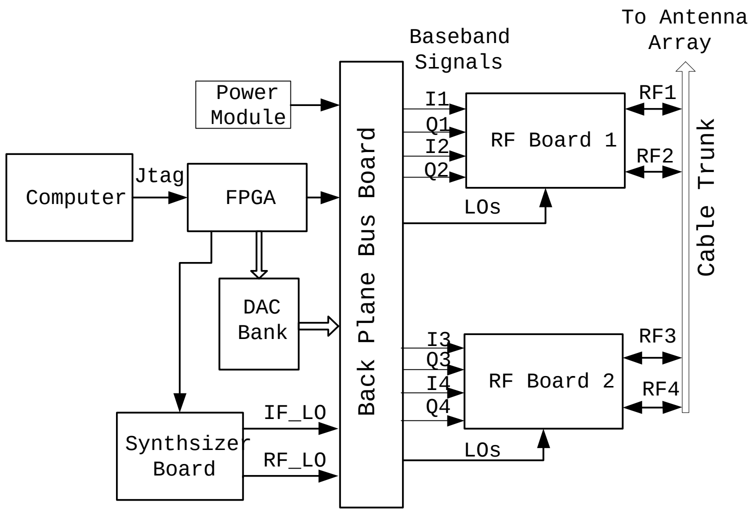

Figure 3.7: Block diagram of transmitters

defined as before. The length of the probing data sequence amounts to 752 points, a value that is designed to fit in the memory of the FPGA. Four sets of I and Q data sequences are output synchronously from the FPGA to four dual-channel DACs with a chip frequency of 10 MHz. Consequently, the period of the probing signal is 75.2μs. A picture of the FPGA board is shown in Figure 3.8.

In the baseband signals, any frequency components higher than 2.5 MHz are removed by the active low-pass filters to avoid aliasing. Those four filtered baseband signals are modulated with an intermediate-frequency (IF) local oscillator signal. They are then up-converted to the radio frequency (RF) of 1.8 GHz. Very stable LO signals are synthesized by a phase lock loop (PLL). The local oscillator in the synthesizer board provides the intermediate frequency LO_{IF} = 138.625 MHz and a very stable radio frequency LO_{RF} = 1.647 GHz, with programmable function scanning from 1637 MHz to 1672 MHz. The RF signals of all transmitters are amplified up to 27 dBm at the front ends. Be-

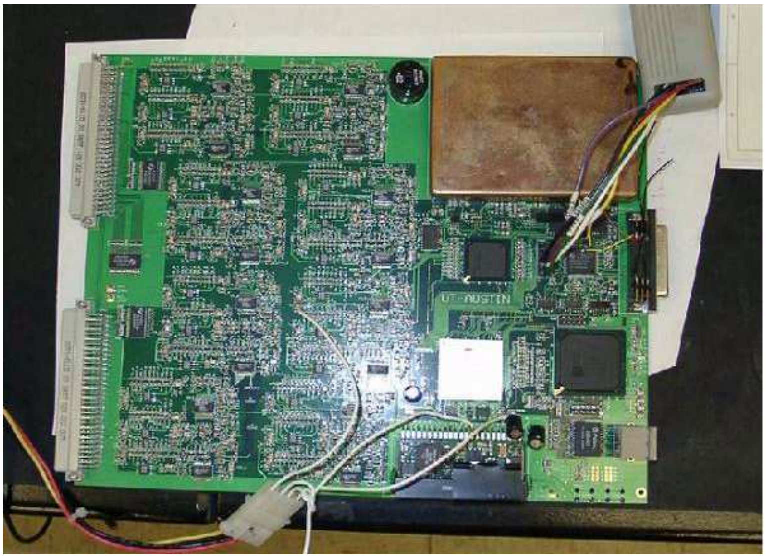

Figure 3.8: Picture of FPGA board

cause of the losses in the coaxial cables and component discrepancies among the Tx modules, the four RF signal strengths are not exactly at the same level in practice. Consequently, we have to remove those differences by calibration. The basic schematics of RF circuitry are shown in Figure 3.9, and a picture of the RF board is shown in Figure 3.10. Each PCB contains two Tx modules; therefore, we need two RF boards to achieve four transmitters in the wideband MIMO channel sounder.

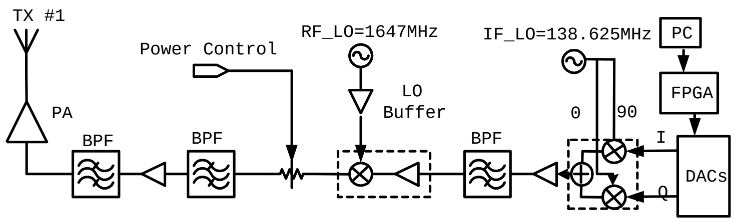

Figure 3.9: Schematic of transmitter

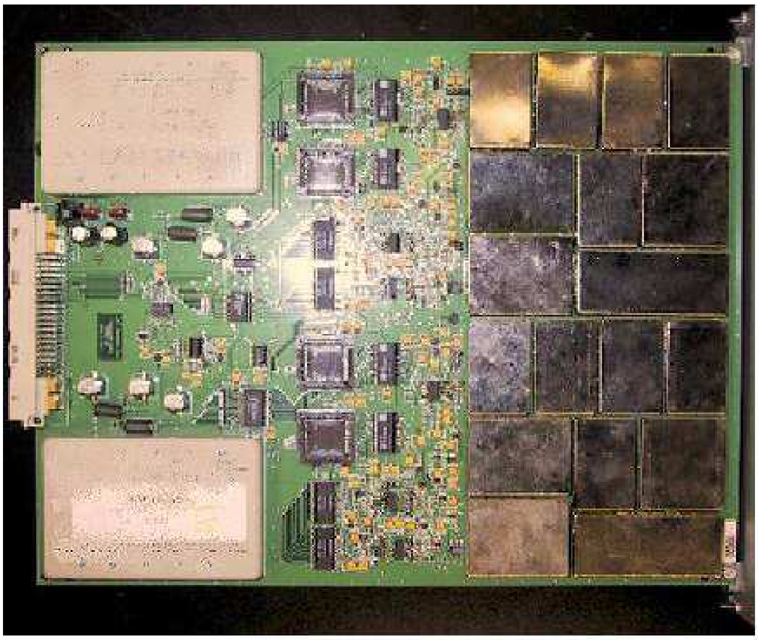

Figure 3.10: Picture of the RF board

3.3.2 Receiver

The Rx testbed consists of eight identical receiving modules, one PLL synthesizer board, four National Instruments data acquisition cards (DAQ) with a personal computer, and one FPGA control unit. The block diagram of the Rx testbed is shown in Figure 3.11. The Rx local oscillators are generated by the PLL in the same way as the Tx testbed. In practice, it is almost impossible to synchronize the Tx carrier frequency and the Rx carrier frequency all the time. For that reason, we have to estimate the offset frequency during post data processing. In the Rx modules, all signals received by the RX antennas are first down-converted to IF signals. They then go through the mixers to be demodulated into eight I and Q baseband signals. A schematic of the I and Q demodulation and down-converter is shown in Figure 3.12.

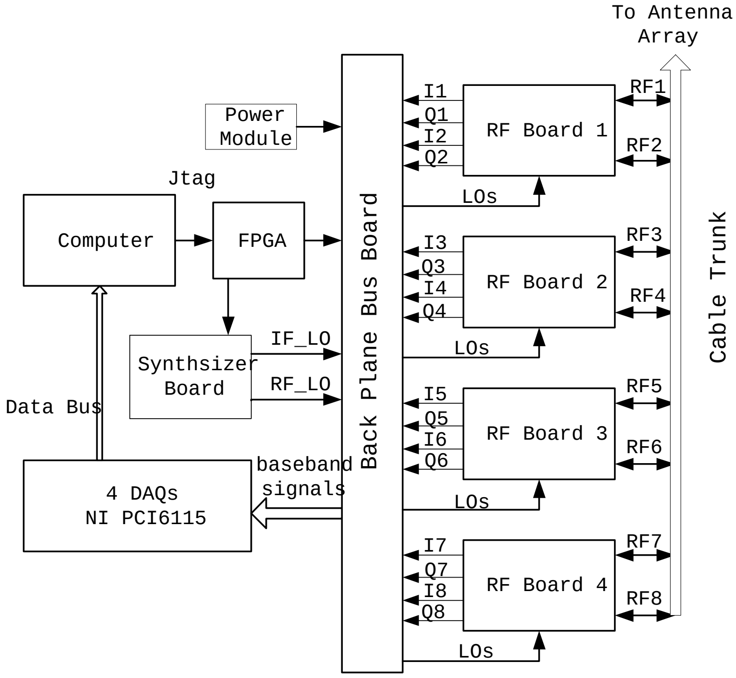

Figure 3.11: Block diagram of receivers

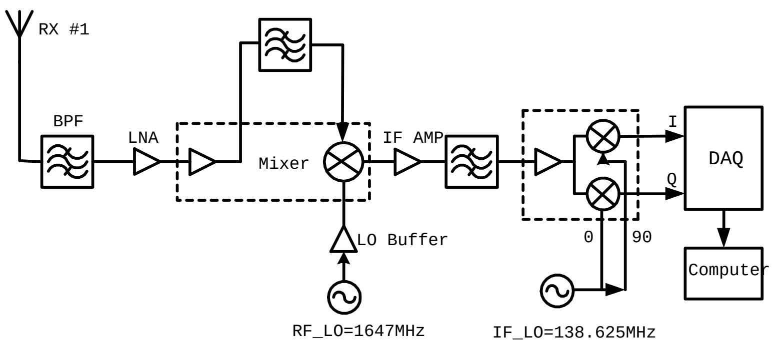

Figure 3.12: Schematic of receiver

The PCB of the FPGA module in Figure 3.13 is designed with six layers of FR4 dielectric substrate, because the module must combat much interference from digital and analog signals. There are one interior layer assigned for the digital ground and the analog ground and another interior layer for the positive power and the negative power supply. Minimum signal traces are 5 mil for affordable PCB fabrication.

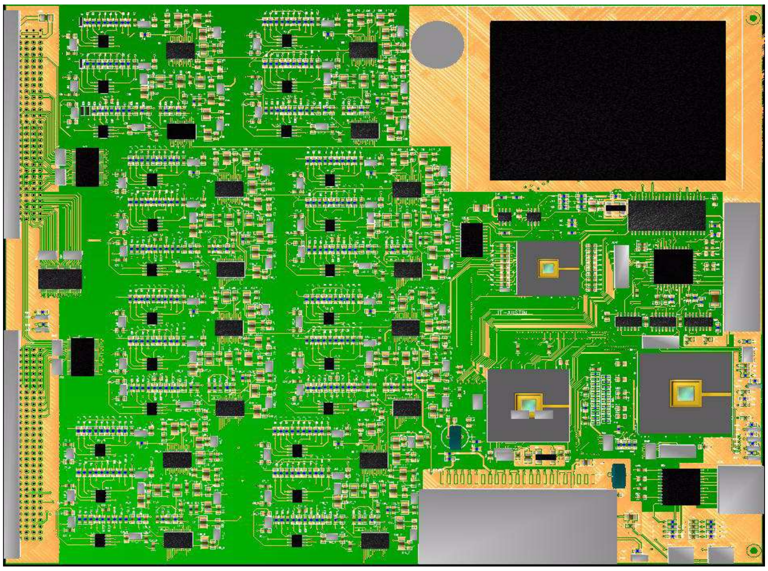

Figure 3.13: Sample of printed circuit board

The RF PCB of the receivers is fabricated in the same way as that of the Tx module. All baseband signals are sampled simultaneously at a rate of 10 MHz and digitized at a 12-bit resolution by National Instrument data acquisition cards (PCI-6115). Four DAQ cards in the computer collect the channel data onto the hard drive for post-processing. Because each DAQ card has 32 M samples of on-board memory, the maximum time for a snapshot goes up to 100 ms with the highest sampling rate. Figure 3.14 shows the wideband MIMO channel receiver inside a van during the measurements.

Figure 3.14: Picture of receiver testbed

Note that the maximum excess delay that can be measured by our testbed is $12\mu s$, which is determined by the PN probing sequence and the chip rate of 10 MHz. The minimum resolvable delay is $0.4\mu s$ due to the sampling rate of 10 MHz and the four-time over-sampling. Thus, the bandwidth of the baseband signals is 2.5 MHz, which translates into $0.4\mu s$ of resolvable delay.

3.3.3 Local Oscillator Synthesizer

A super stable LO is very important to the transmitter and receiver, because synchronization between Tx and Rx is critical to the modulation and demodulation of the communication system. Figures 3.15 and 3.16 show the diagram of phase lock loop of IF and RF local oscillator generators based on LMX2330 chip. A 12 MHz reference crystal is used. Therefore, the IF LO is 138.625 MHz, while the RF LO is 1647 MHz.

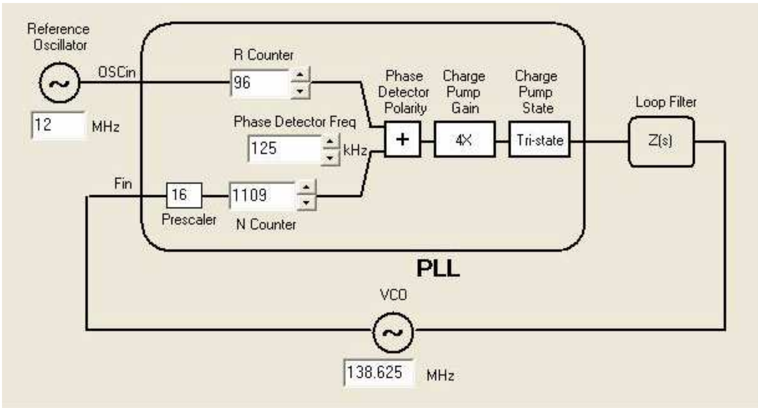

Figure 3.15: Diagram of IF LO generator

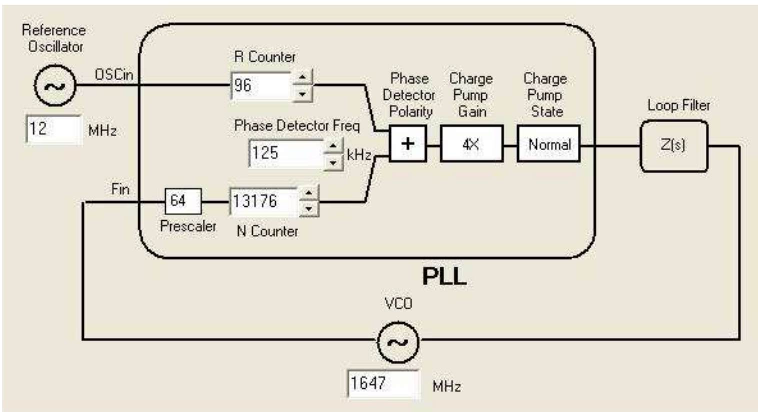

Figure 3.16: Diagram of RF LO generator

The serial port with clock signal, data stream, and enable signal are accomplished by FPGA. Figure 3.17 shows the structure of four 22 bits, which are used by the synthesizer board.

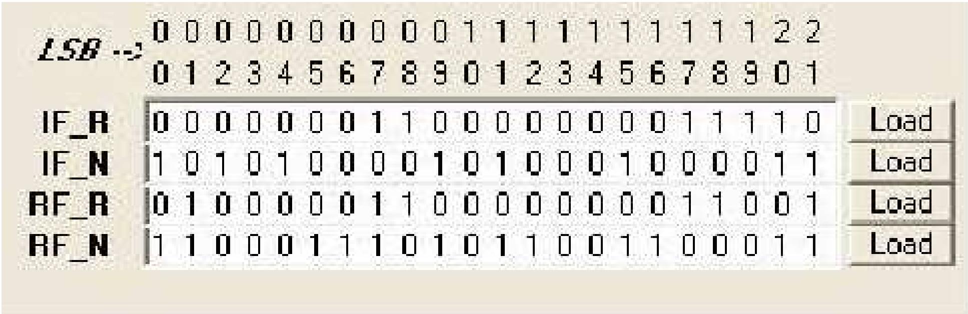

Figure 3.17: Data stream of serial port

3.3.4 Antenna Array

The transmitters radiate RF signals by means of a uniform linear array (ULA) with four antenna elements, and the element spacing of the Tx array is fixed at 1λ, where λ is the radio wavelength. The Tx antenna array is shown in Figure 3.18. The array elements are quarter-wave length monopoles. The receivers use a ULA with eight antenna elements, and the element spacing of the Rx array is adjusted to either 0.5λ or 1λ for different measurement setups. The Rx antenna array is shown in Figure 3.19. The Rx array elements are co-linear dipoles. The Rx testbed is carried inside a van, and the Rx antenna array is mounted on a wooden stand.

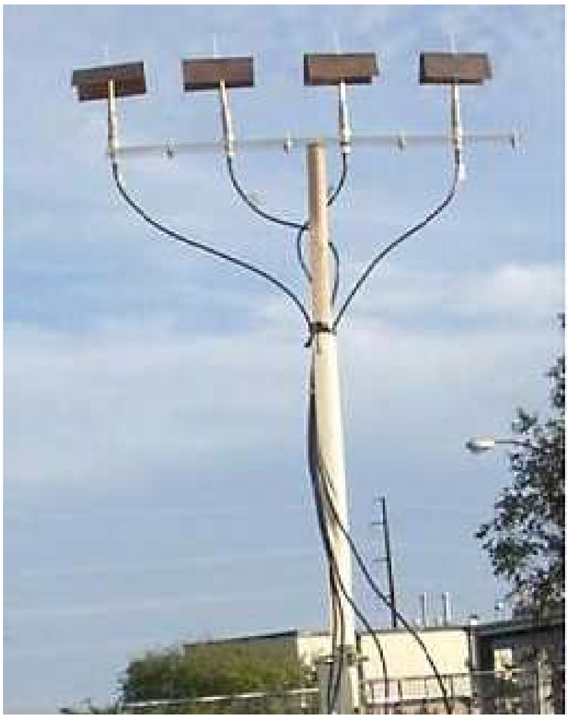

Figure 3.18: Picture of transmit antenna array with four elements

Figure 3.19: Picture of receiver antenna array with eight elements

3.4 Software of Wideband MIMO Channel Sounder

3.4.1 VHDL for FPGA

VHDL is a hardware descriptive language that is used widely for FPGA applications. In both transmitter and receiver testbeds, different VHDL codes are simulated, and their corresponding bit files are downloaded. State machines are designed to satisfy the special requirements for either the transmit or receive testbed.

Since LOs are needed for both Tx and Rx, a common VHDL code is created as a serial port so as to generate the same IF LO and RF LO. In practice, LOs may be a little different at the Tx side that at the Rx side. LO offset correction is needed during postprocessing.

In the Tx testbed, the probing sequences are continuously and synchronously output to the DAC by FPGA. Thus, timing issues become critical when data rates reach as high as 10 MHz. This problem poses a challenge to PCB design and VHDL programming. During the downloading of the bit files, field tests and debugging are carefully monitored with an oscilloscope, because the waveforms may be seriously distorted. Tx power control can be programmed by FPGA. A simple dual four bits DAC is designed to fulfill purpose. Similarly, receive gain controls in Rx testbed are also furnished by FPGA through DAC.

3.4.2 LabVIEW VI for Data Acquisition

LabVIEW is a data-flow-based graphical programming language that provides the user with simple programming and rapid prototyping capabilities. At the receiver, four National Instruments PCI 6115 data acquisition cards are used. Each card comes with an I/O box with four analog signal inputs. In terms of hardware, to sample the analog signal simultaneously, a special synchronization ribbon cable is applied to the four cards. Thus, simultaneous receiving of the system is guaranteed when the virtual instrument file is created accordingly. The sampling rate and the number of samples can easily be adjusted by creating proper sub VI. During the measurements, a maximum sampling rate of 10 MHz and a reasonable 10,000 samples are configured. Thus, each snapshot data is a 10,000 by 16 matrix that will be assigned a unique file name for later analysis. A block diagram of DAQ in LabVIEW is shown in Figure 3.20. The front panel of another version of synchronized DAQ in LabVIEW is shown in Figure 3.21.

3.4.3 Data Processing by Matlab

Raw data collected by the spread-spectrum technique are processed to obtain estimates of the time-variant channel matrix. Postprocessing is done by Matlab. The technique usually consists of three basic steps: sequence synchronization, carrier recovery, and channel estimation [37].

• **Sequence Synchronization by Serial-Searching:** Since the time instance of activating a snapshot is arbitrary during the data collection, locating the start point of the signal sequence is important. A popular strategy for the acquisition of spread-spectrum signals is to use a signal correlator or

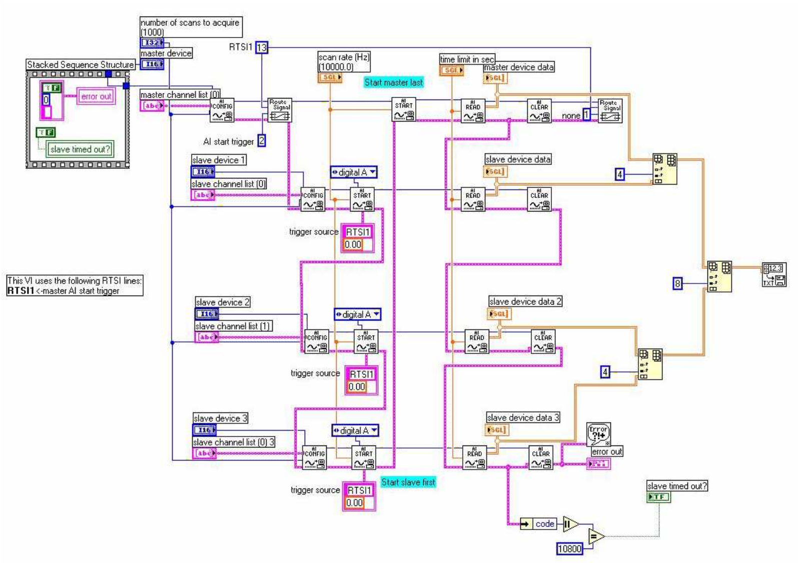

Figure 3.20: Block diagram of DAQ

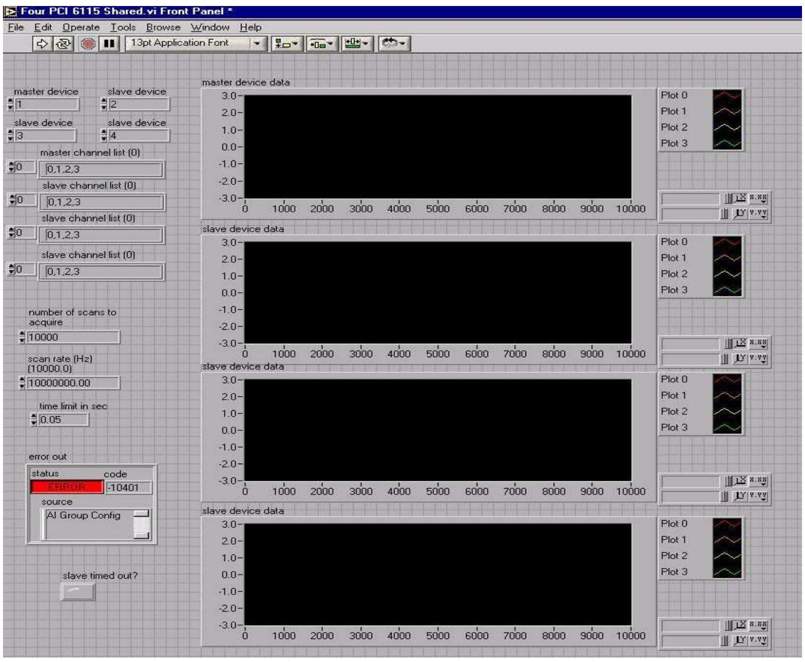

Figure 3.21: Front panel of LabVIEW DAQ

a matched filter to serially search for the correct phase of the sequence. A considerable reduction in complexity, size, and cost can be achieved by a serial implementation that repeats the correlation procedure for each possible sequence shift. Thus, we begin by correlating the signal from one of the M_R receive antennas with the base PN probing sequence. A high correlation peak emerges if the sequences in the receive signal are aligned. Additionally, if the received signal is too weak, the maximum correlation may not occur at sequence alignment. To overcome this pitfall, our procedure searches every combination of receive channel and sequence to ensure accurate synchronization.

- **Carrier Recovery:** In our channel sounder, systematic frequency offsets that are caused by LO mismatches between the transmitter and receiver are estimated and compensated. This removal is necessary because carrier frequencies of about 1.8 GHz typically have offsets that range up to a few kHz after system power is turned on. The offset is estimated through the phase variation of all the received signals after searching the maximum cross-correlation within the first two periods of the data points. It is reasonable to assume that static offsets exist in the system. The estimated frequency offset is used to compensate for all of the received signals by adding a relative phase [49]. To estimate such a carrier offset, a digital rotator is multiplied to the PN sequence during calculation of the cross-correlation between the received signals and the base PN probing sequence. Once the maximum correlation is detected, we can determine the offset frequency.

Another assumption is that we do not have any stronger delayed signals with more than 12μs delay time during the measurement. This assumption is reasonable, because we use relative low power transmission, and any signals will be attenuated significantly after many reflections or long-distance travel. In this way, we can simplify the process of the channel estimation.

- **Channel Estimation:** In a wireless communication system, the channel is usually time-varying and unknown to the receiver. Thus, the channel estimation is updated periodically by the communication system. In our implementation, we transmitted four periodic probing signals, and a maximum usable channel length is 120 data points. Thus, 30 taps, or 12μs, for each Tx-Rx link was assumed. The channel impulse responses are extracted off line by the cross-correlation of the received data sequence with the base PN probing sequence. Because the PN probing sequences are not orthogonal, it is necessary to perform an inversion to extract the complex channel transfer matrix from the measured data.

3.5 Calibrations of Channel Sounder

As mentioned, the performances of the RF components, the cable losses, Tx power control, and Rx receive gain control generally vary over frequency and temperature. At the preliminary stage of the testbed, the four transmitters did not output the power level desired, and the phase between the in-phase and quadrature branch were not $90°$. For those reasons, hardware adjustments have to be made [50]. For example, by monitoring the output power at the end of the cable to a Tx antenna via a spectrum analyzer (as shown in Figure 3.22), we can compare the output power levels of the four transmitters and make them close to the maximum power level. By generating a sine wave and a cosine waveform as the I and Q baseband sequences to the Tx modules, we can monitor the output spectrum and correct the phase error within the frequency bandwidth of interest by adjusting its in-phase and quadrature balance. For the Rx module, a CW is input at the front end, and the phase error can be corrected by adjusting the I and Q balance such that a circle on the oscilloscope responds to the I and Q inputs. In this way, the hardware trim adjustment minimizes the difference between the transmitter module and the receiver module.

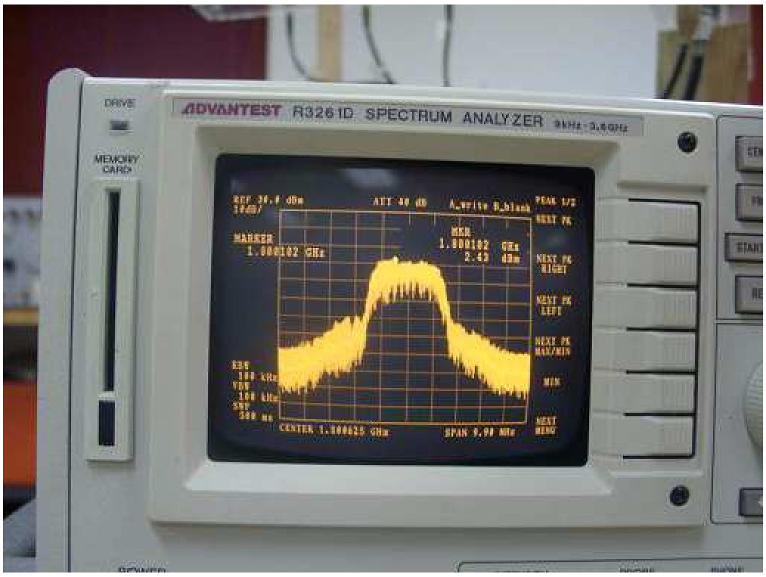

Figure 3.22: Measured spectrum of the transmitted signal

- *Basic calibration*: The setup for the calibration is shown in Figure 3.23. The calibration procedure of Tx1 to Rx1 begins with the insertion of an attenuator between the Tx1 cable and the Rx1 cable. All other cables should be terminated. The attenuator should have flat response over the frequency bandwidth of interest. For instance, Kay Elemetrics Corporation's 839 is a good choice with a loss variation of 0.15dB within the operating frequency band from 1.7 GHz to 1.9 GHz.

Figure 3.23: Picture of calibration procedures

During the calibration, the probing sequences are used instead of continuous wave (CW). To measure the radio environments at a large distance, the Tx output power is configured to the maximum. Various attenuation values, such as 70 dB, 75 dB, 80 dB, and 85 dB, are used to simulate the distance variations. Receive gains are then determined accordingly to avoid input saturation while maintaining proper sensitivity. The receiver gain values are stored in the FPGA for selection during the measurement at a specific environment. For example, in most LOS measurements, a low Rx gain is sufficient because the received signals are usually strong. In contrast, in the far NLOS environments, the received signals are extremely weak, and a high Rx gain is required to detect those signals.

At the end of this basic calibration, Tx1 and Rx1 are treated as the reference when calibrating the other transmitters and receivers.

- *4 Tx calibration*: The objective is to remove the differences among the four transmitters. During this procedure, Rx1 is chosen as the reference receiver, and the calibration of Tx2, Tx3, and Tx4 is performed in the same way as the basic calibration by replacing Tx1 with Tx2, Tx3, and Tx4, respectively. Comparison with the correlation result of Rx1 and Tx1 at the same attenuation value yields the differences between all other transmitters with respect to Tx1. Those differences are then stored for data postprocessing. Hence, after compensation of the differences, all four transmitters are supposed to be identical, except they are at different positions in the Tx array.

- *8 Rx calibration*: The objective is to remove the differences among the eight receivers. During this calibration precess, Tx1 is chosen as the reference transmitter. By replacing the Rx1 with Rx2, Rx3, etc., the calibration is performed in the same way as the basic calibration described above. Comparison with the correlation result of Rx1 and Tx1 at the same attenuation value yields the differences among all seven receivers with respect to the Rx1. Those differences are then stored for data postprocessing. Hence, after compensation of the differences, all eight receivers are supposed to be identical, except they are at different positions in the Rx array.

In all, these calibration procedures should be carefully performed prior to the field measurement to exclude the influence of the system on the measured data. In the calibration, Tx and Rx antennas are not used. Instead, cables and an adjustable attenuator are used to couple the Tx and Rx. Theoretically, the power transfer function of the measurement setup should be flat over the measured frequency range. Since the antennas are not present during the calibration process, their effects have to be treated as environmental. Let us consider the basic calibration and denote the various transfer functions as follows: $H_{measured}$ is the measured transfer function, H_{no_cal} is the measured transfer function without calibration, H_{cal} is the calibration transfer function, $H_{Tx\_amp+cables}$ is the transfer function of the Tx amplifier and cables, $H_{Tx\_antenna}$ is the transfer function of the Tx antenna, $H_{Rx\_preamp+cables}$ is the transfer function of the Rx pre-amplifier and cables, $H_{Rx\_antenna}$ is the transfer function of the Rx antenna, $H_{channel}$ is the transfer function of the channel, and $H_{attenuator}$ is the transfer function of the attenuator. $H_{measured}$ can be expressed by the following formula:

$$\begin{aligned} H_{measured} &= \frac{H_{no\_cal}}{H_{cal}} \\ &= \frac{H_{Tx\_amp+cables} \cdot H_{Tx\_antenna} \cdot H_{channel} \cdot H_{Rx\_antenna} \cdot H_{Rx\_preamp+cables}}{H_{Tx\_amp+cables} \cdot H_{attenuator} \cdot H_{Rx\_preamp+cables}} \\ &= \frac{H_{Tx\_antenna} \cdot H_{channel} \cdot H_{Rx\_antenna}}{H_{attenuator}} \\ &\propto H_{channel} \end{aligned} \tag{3.1}$$

Equation 3.1 shows that, in addition to the influence of both the Tx and Rx antennas, the channel measurement results are still influenced by the impact of the attenuator. However, if the attenuator has a flat frequency response, the influence can be neglected. Consequently, the antennas have to be treated as parts of the environment of the wireless channel.

3.6 Summary

The wideband MIMO channel sounder was successfully designed and implemented, which operated at 1.8 GHz with a bandwidth of 2.5 MHz. We also have conducted two confidence tests. The first confidence test was to generate an echo with 120 m long cable to emulate a LOS signal with a power coupler. The wideband probing sequence was transmitted. In the received signals, two correlation peaks with noticeable delay were correctly observed; one was the LOS and the other was the echo signal. The second test was to check the multipath delay profile at a fixed location with different probing antenna. For every test, the delay profile was indistinguishable from the other testing result due to the consistency of the system. In all, the wideband testbed performed robustly during the field measurements. The specifications of the wideband MIMO channel sounder is summarized in the Table 3.1.

Table 3.1: Specs of wideband MIMO channel sounder.

Measurement frequency	1.8 GHz
Chip rate	10 MHz
Delay resolution	0.4μs
Bandwidth	2.5 MHz
Probing signals	Pseudo-random noise
Number of Tx antenna	4 element ULA
Element spacing	1λ
Number of Rx antennas	8 element ULA
Element spacing	0.5λ or 1λ

Chapter 4

Measurement Campaigns and Channel Characteristics

This chapter addresses channel estimations and field measurements of wideband vector channels and matrix channels in outdoor environments. Different antenna array configurations are used to collect channel data with the true array channel sounder in LOS and NLOS environments. Multipath delay profile are extracted, and root mean square (RMS) delay spreads are compared according to the measurement scenarios. Statistics of matrix channel elements are studied. Before we describe the field measurements, the raw-data processing is discussed first so that we can show the measurement results accordingly.

4.1 Descriptions of Radio Environments

Figure 4.1 shows the layout of the measurement scenario at the J. J. Pickle Research Campus, The University of Texas at Austin. There are about 50 buildings within this area. Most of the buildings are one or two stories high, and they are labelled by numbers. The Tx antenna array was located at Tx_Loc on the roof of Building16, which is 6 m above the ground. For non-line-of-sight channel measurements, the Rx array stood on the ground west of Building MER160, where the spots of Rx_Loc1 and Rx_Loc2 were located for the measurement campaigns.

Because Building MER160 is a comparatively tall building at 25 m in height, it completely blocks the direct path from the Tx to the Rx. The distance between Tx_Loc and Rx_Loc1 is approximately 200 m without the blockage of MER160, and the distance between Tx_Loc and Rx_Loc2 is approximately 320 m without the MER160 blockage. On the south side of the PRC, a row of buildings (not shown in the figure) and other buildings within this area produce the reflective radio paths. There are many trees and much grassland that may influence the signal strength. For LOS channel measurements, the Rx array is set up at the Rx_LOS site. The Tx-Rx separation is around 150 m. No blockage exists in-between in this case, but the reflected waves from nearby objects are in effect. Figure 4.2 shows a picture of the Rx antenna array at Rx_Loc1. Inside the van is the Rx testbed to take channel data.

Channel data are collected based on the snapshot at different locations. A snapshot records 10,000 data points for each Rx baseband signal. The sampling rate is 10 MHz, and one period of the probing signal is 752 data points; therefore, one snapshot acquires $\lfloor 10000/752 \rfloor = 13$ periods of baseband PN probing sequence. For reliability, we use 12 periods during the data analysis.

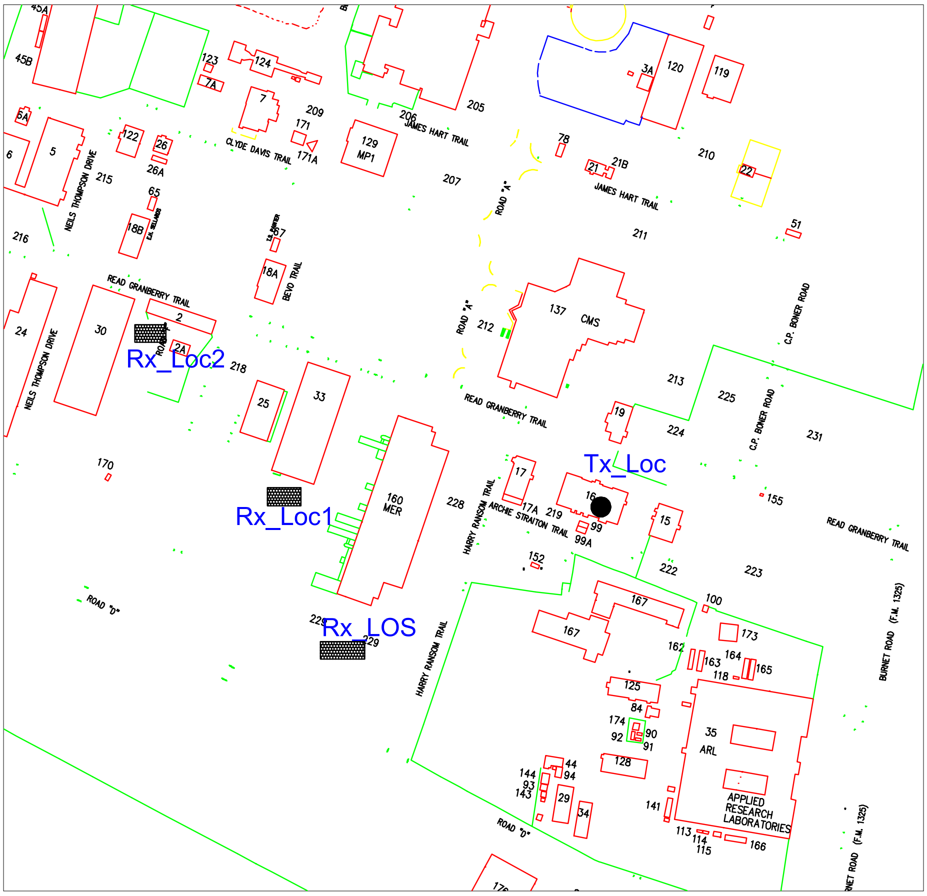

Figure 4.1: Measurement environment.

Figure 4.2: Picture of field measurements

4.2 Measurements of Wideband MIMO Channels

To study the wideband MIMO channel features, measurements according to the antenna array locations, environments, and intra-element spacing are conducted. Since channel impulse responses change dramatically over a small displacement of array location in the multipath environments. Thus, it is necessary to examine the characteristics of the matrix channel associated with the array displacement.

4.2.1 Data Collection of LOS Channel

The location of the Tx antenna array is fixed on the roof of Building 16, but the position of the Rx antenna array stand is moved over a distance of at least 10λ on the ground. In the LOS measurement, the Rx is located between Building 16 and Building MER160, where the site RX_LOS is shown as in Figure 4.1. The Tx-Rx separation was about 150 m.

First, the intra-element spacing Δ of the Rx antenna array is set to be 0.5λ. The initial position of the Rx array is selected arbitrarily during the measurement. A snapshot is taken when the Rx antenna array is moved by a small step of 0.1λ. For reliability, three measurements are taken while the Rx array remains in the same location. Therefore, the set of channel data over the distance of 10λ consists of 303 snapshots, which amounts to 3636 samples of channel response matrices. Secondly, the Rx antenna intra-element spacing is adjusted to 1λ, and all of the measurements are repeated according to the same procedure as that of $\Delta = 0.5\lambda$. This generates another set of data with 303 snapshots.

The procedure of the data collection is depicted in Figure 4.3. Figure 4.4 shows the overlapped curves of the 12 profiles in one snapshot. Notice that 32 small humps were obtained. Actually, the x-axis is a multiplexed time scale resulting from four transmitters, the y-axis is the discrete number of Rx receivers, and the z-axis is the relative multipath intensity profiles. Observe that there are no strong reflected signals, but the different peaks of the 32 curves show the vector addition of the signals of the direct path and multipaths.

4.2.2 Data Collection of NLOS Channels

The following two case studies are conducted to investigate the channel data for NLOS channels.

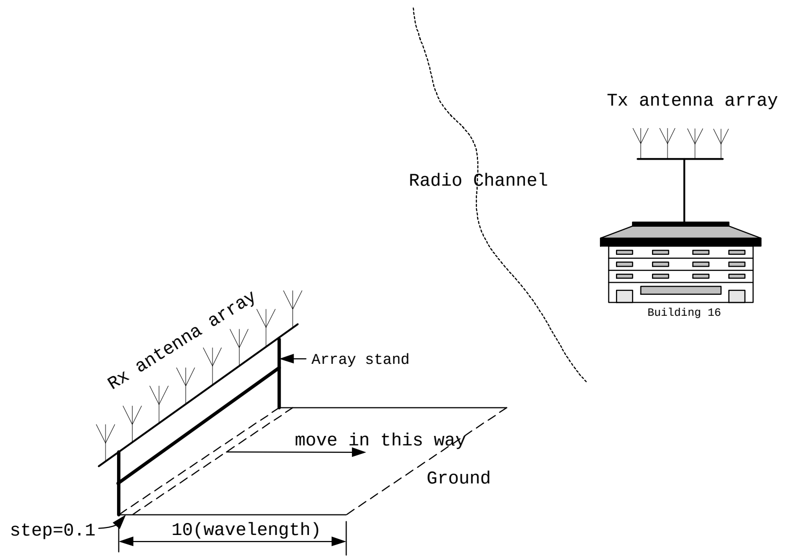

Figure 4.3: Procedure of data collection.

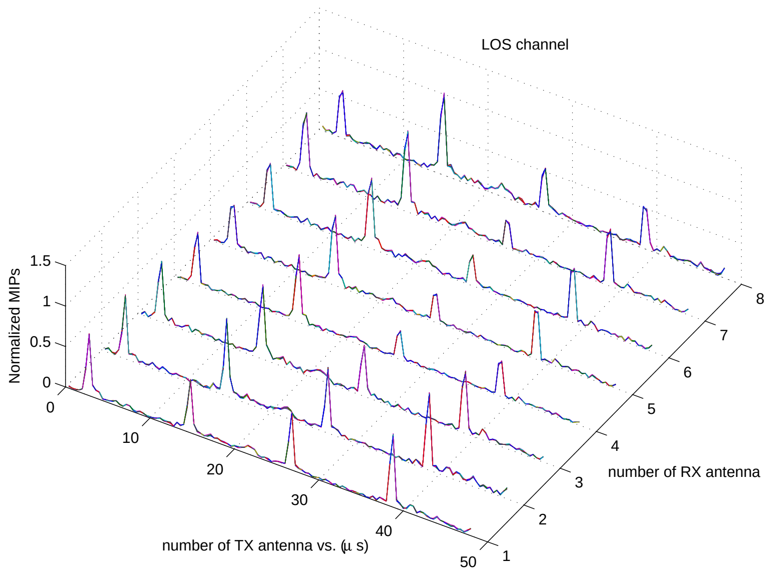

Figure 4.4: Example of multipath intensity profiles (MIP) of LOS channel.

- Case Study 1: The position of the Tx antenna array is fixed on the roof of Building 16, but the position of the Rx antenna stand is moved over a distance of 10λ. First, the Rx antenna array with intra-element spacing $\Delta = 0.5\lambda$ is set at the spot of Rx_Loc1. The initial position of the Rx array is selected arbitrarily. A snapshot is taken when the Rx antenna array is moved by a step of 0.1λ. The data collection procedure is the same as that depicted in Figure 4.3. For reliability, three measurements are taken while the Rx array stays at the same location. Therefore, a set of channel data over the distance of 10λ consists of 303 snapshots, which amounts to 3636 channel impulse responses. Second, the Rx antenna spacing is adjusted to 1λ, and all of the measurements are repeated by the same procedure as that of $\Delta = 0.5\lambda$. Another set of data with 303 snapshots is generated accordingly. Third, the Rx testbed is moved to the site of Rx_Loc2, and the same measurement procedures are repeated as those at Rx_Loc1. Thus, there is a total of $303 \times 4 \times 12 = 14,544$ channel impulse response matrices associated with the Rx array locations, Rx intra-element spacing, and two different NLOS scenarios. Figure 4.5 shows an example of the wideband MIMO multipath delay profiles in a NLOS scenario.

- Case Study 2: The location of the Rx antenna array is fixed at Rx_Loc1 and Rx_Loc2 with intra-element spacing of 0.5λ or 1λ, respectively. However, the orientation of the Tx antenna array is controlled by a motor with an angle step of $360°/100 = 3.6°$, which means that after 100 steps, the Tx array returns to its initial position. At each orientation of the Tx array, three snapshots of measurements are taken. The measurement

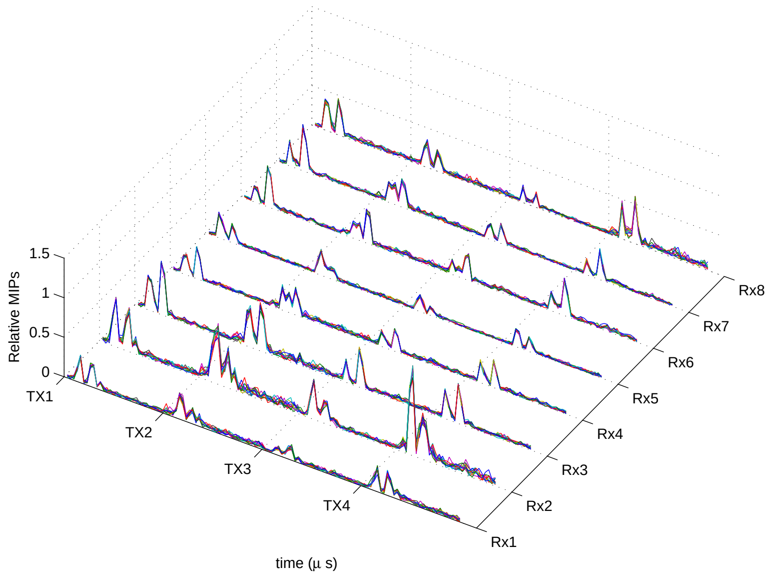

Figure 4.5: Example of multipath intensity profiles (MIP) of NLOS channel. Tx array locates on the roof of Building 16, Rx array locates on the west of Building MER 160, with intra-element spacing of 1λ

procedures are similar to those in case study 1. Finally, a total of 14,544 channel impulse response matrices of data were recorded. To show the difference of the Tx position during the rotation, the pivotal point is off the center of the ULA array by $1/4$ λ.

4.3 Characteristics of Matrix Channels in NLOS Environments

4.3.1 Analysis of Multipath Delay Spread

The channel impulse responses are extracted from the collected raw data after the application of the calibration coefficients. The mean excess delay and RMS delay spread can be computed based on Equations 4.1 and 4.2 [1].

$$\bar{\tau} = \frac{\sum_k P(\tau_k)\tau_k}{\sum_k P(\tau_k)} \tag{4.1}$$

where k is the tap index and $P(\tau_k)$ is the relative power level of multipath component at delay τ_k. The rms delay spread is the square root of the second central moment of the power delay profile given by

$$\tau_{rms} = \sqrt{\overline{\tau^2} - (\bar{\tau})^2} \tag{4.2}$$

where

$$\overline{\tau^2} = \frac{\sum_k P(\tau_k)\tau_k^2}{\sum_k P(\tau_k)} \tag{4.3}$$

The inverse of the rms delay spread is referred to as the *coherence bandwidth* (B_c) of the channel. Coherence bandwidth is the range of frequency over which two frequency components have a strong potential for amplitude correlation. A signal undergoes frequency selective fading if the signal bandwidth (B_s) is wider than the coherent bandwidth, and the symbol period (T_s) is less than the rms delay spread (τ_{rms}). A rule of thumb is that a channel is non-frequency selective if $T_s \geq 10\tau_{rms}$, and a channel is wideband if $T_s < 10\tau_{rms}$. The coherence bandwidth is inversely proportional to the delay spread and characterizes the channel's frequency selectivity. Typical values of the delay spread are $0.2\mu s$, $0.5\mu s$, and $3\mu s$ for rural areas, suburban areas, and urban areas, respectively [13].

RMS delay spread is decided by many factors, such as the Rx location, Rx antenna intra-element spacing, Tx positions, and the environment. Figure 4.6 shows the power delay profiles of one snapshot in case study 1, which results from averaging over $12 \times 32 = 384$ multipath intensity profiles.

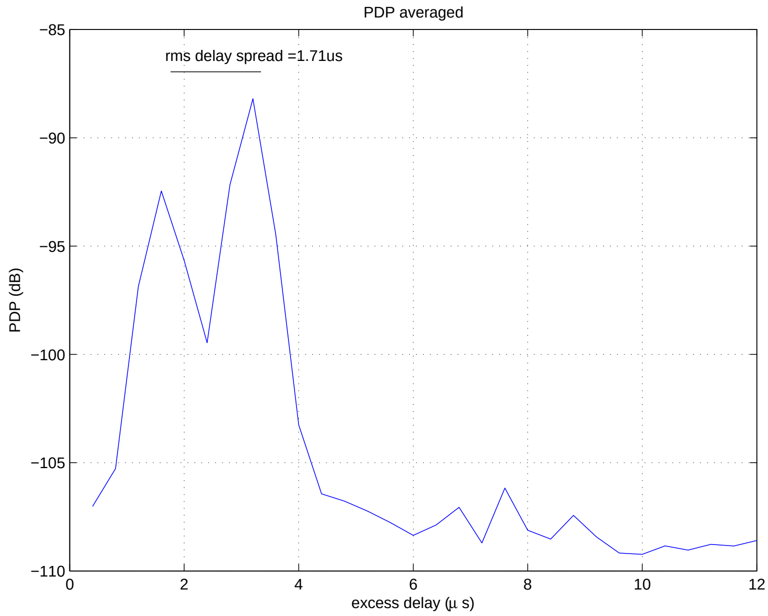

Figure 4.6: Power delay profiles at Rx_Loc1 given the intra-element spacing of 0.5λ.

Because the power delay profile is the averaged value of the multipath delay profiles over time and space, the RMS delay spread from the PDP is different from RMS delay spread from multipath delay profiles. Figure 4.7(a) shows the probability density function of all τ_{rms} based on snapshot at Rx_Loc2 and $\Delta = 0.5\lambda$ in case study 1. The result is very close to the normal distributions [51, 52]. Figure 4.7(b) shows a CDF of RMS delay spread calculated from the multipath delay profiles at each Rx location. It is easy to verify that the RMS delay spread calculated from all the other sets of measured data has a similar distribution. Figure 4.8 shows the cumulative density function of τ_{rms} calculated from the power delay profiles averaged over time, space, and locations in case study 1. Note that the RMS delay at Rx_Loc1 is bigger than that at Rx_Loc2 in case study 1.

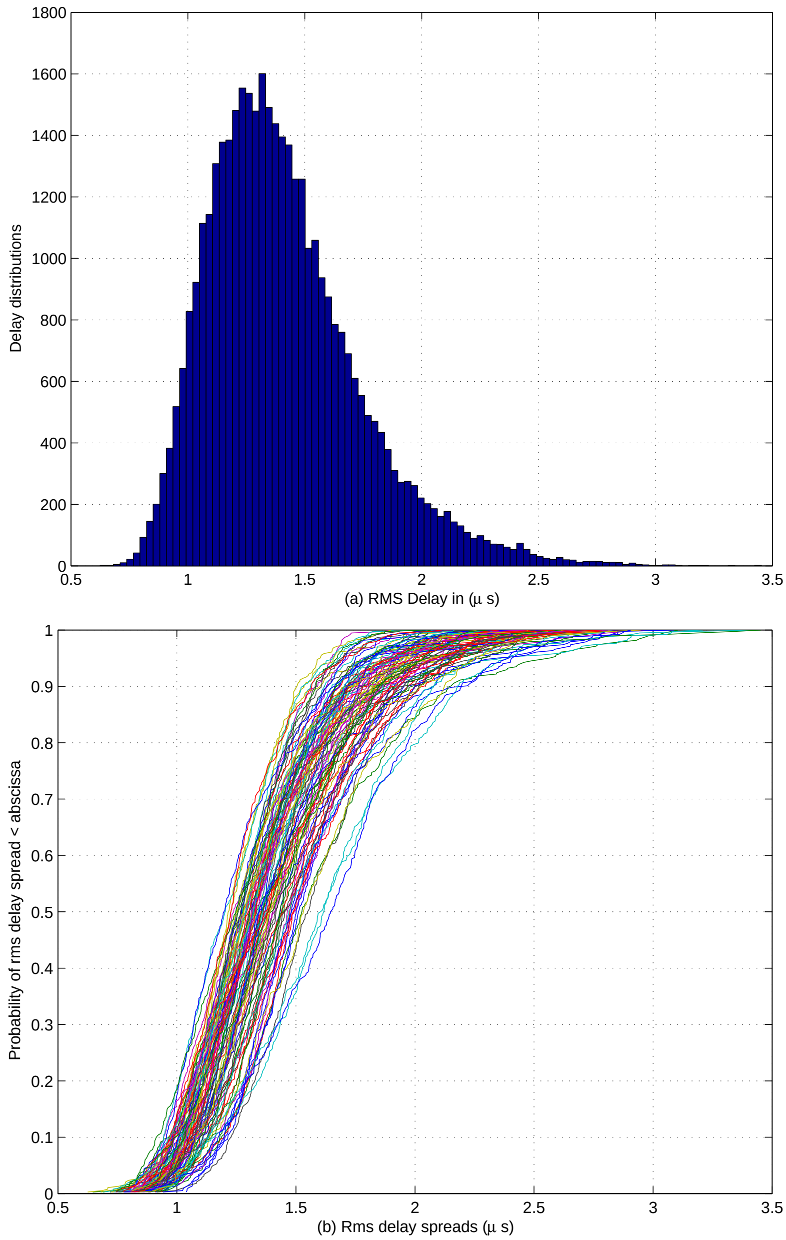

Figure 4.7: The empirical distributions of RMS delay spread over 10λ. (a) Histogram of RMS delay spread. (b) RMS delay spread calculated based on 101 locations.

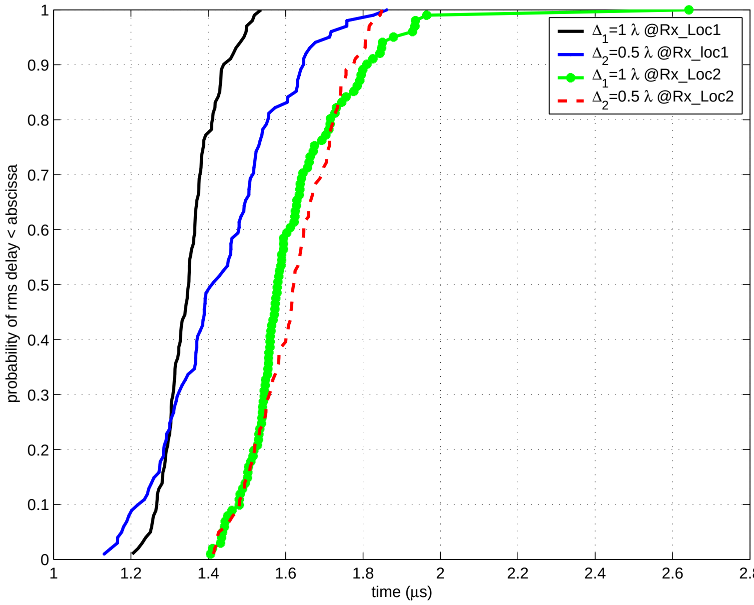

Figure 4.8: CDF of RMS delay spread over 10λ.

Table (4.1) shows the normal distribution parameters of τ_{rms} in case study 1, when the position of the Tx array is fixed and the location of the Rx array is changed.

Table (4.2) shows the normal distribution parameters of τ_{rms} in case study 2, when the location of the Rx array is fixed and the Tx array is spinning in one circle horizontally.

In Tables of 4.1 and 4.2, $\hat{\tau}_1$, $\hat{\tau}_2$, and $\hat{\tau}_3$ denote the mean of τ_{rms} for three repeated measurements when Tx array and Rx array are kept in the same location; $\hat{\sigma}_1$, $\hat{\sigma}_2$, and $\hat{\sigma}_3$ are the variances of τ_{rms}; and $\bar{\tau}$ and $\bar{\sigma}$ are the average of $\hat{\tau}$ and $\hat{\sigma}$ over the three measurements. In the NLOS measurements, the RMS delay spread is 1.3139$\sim$1.5821μs with the variance of 0.2966$\sim$0.3754μs. Notice that the RMS delay spread calculated from the averaged power delay profile is slightly larger than the mean of RMS delay spread calculated from

Table 4.1: Statistical parameters of $\tau_{rms}(\mu s)$ in case study 1

	Rx_Loc 1		*Rx_Loc 2*	
Δ	0.5λ	1λ	0.5λ	1λ
$\hat{\tau_1}$	1.5887	1.5017	1.4073	1.3910
$\hat{\sigma_1}$	0.3724	0.3298	0.3265	0.3706
$\hat{\tau_2}$	1.5652	1.5226	1.4279	1.3745
$\hat{\sigma_2}$	0.3532	0.3368	0.3388	0.3635
$\hat{\tau_3}$	1.5925	1.5088	1.4158	1.3751
$\hat{\sigma_3}$	0.3712	0.3197	0.3361	0.3619
$\bar{\tau}$	1.5821	1.5110	1.4170	1.3802
$\bar{\sigma}$	0.3656	0.3288	0.3338	0.3653

Table 4.2: Statistical parameters of $\tau_{rms}(\mu s)$ in case study 2

	Rx_Loc 1		*Rx_Loc 2*	
Δ	0.5λ	1λ	0.5λ	1λ
$\hat{\tau_1}$	1.5291	1.3728	1.4142	1.3105
$\hat{\sigma_1}$	0.3423	0.3690	0.3222	0.2897
$\hat{\tau_2}$	1.5376	1.3715	1.4160	1.3147
$\hat{\sigma_2}$	0.3529	0.3760	0.3215	0.2982
$\hat{\tau_3}$	1.5359	1.3866	1.4032	1.3166
$\hat{\sigma_3}$	0.3472	0.3913	0.3195	0.3018
$\bar{\tau}$	1.5342	1.3770	1.4111	1.3139
$\bar{\sigma}$	0.3476	0.3754	0.3211	0.2966

the individual multipath delay profiles.

4.3.2 Statistics of Channel Matrix Elements

The marginal probability density function (PDF) for the magnitude and phase of the elements of the channel matrix $\mathbf{H}(f)$ can be derived [37]. These empirical PDFs are computed according to the $\mathbf{H}(f)$ in a frequency bin.

$$p_{magnitude}[x] = \frac{1}{KM_TM_R\delta x} \underbrace{HIST}_{K,M_T,M_R} (abs(H_{mn}^{(k)}), \delta x) \tag{4.4}$$

$$p_{phase}[x] = \frac{1}{KM_TM_R\delta x} \underbrace{HIST}_{K,M_T,M_R} (angle(H_{mn}^{(k)}), \delta x) \tag{4.5}$$

where $HIST(f, \delta x)$ represents a histogram of the function f with bins of size δx, and K is the number of $\mathbf{H}$ matrix samples. In this case, histograms are computed by treating each combination of the matrix sample, the transmit antenna, and the receive antenna as an observation. Figure 4.9 shows the empirical PDFs for the 4×8 MIMO system. These results are compared with the Rayleigh distribution (magnitude) with parameters $\sigma^2 = 0.4$ and the uniform distribution (phase) on $[-\pi, \pi]$. Excellent agreement occurs between the analytical and empirical PDFs. This agreement is a fundamental result for calculating wideband channel capacity by dividing the bandwidth into small frequency bin as described in the next chapter.

4.3.3 Frequency Correlation Features

The frequency response $H(f_i, t)$ computed from the measured samples can be interpreted as a random process [11]. Now the frequency correlation coefficients can be calculated by averaging the channel responses associated with

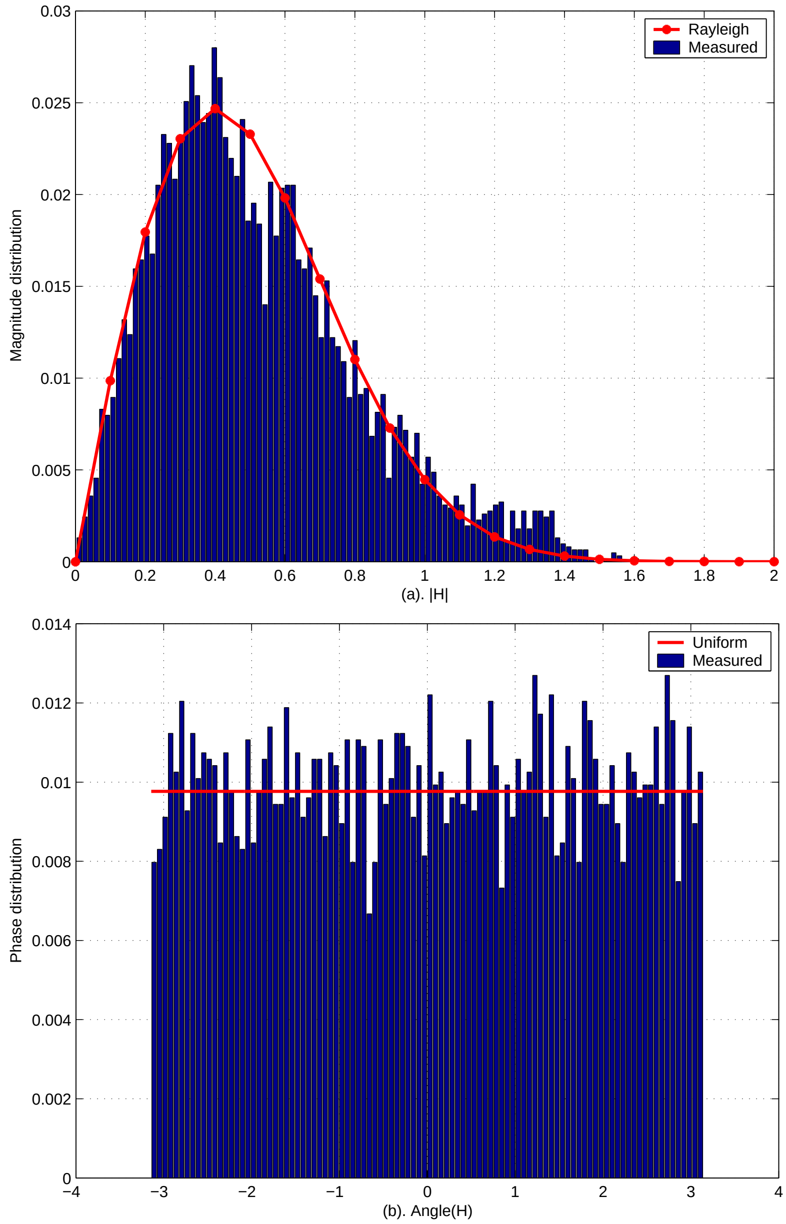

Figure 4.9: Distribution of the elements in channel response matrices based on one frequency bin (narrowband-like) in case study 1

each frequency bin over both time and spatial domains. The autocorrelation function of this process is given by

$$\mathbf{R}(k,0) = \frac{1}{N}\sum_{i=1}^{N-k} h^H(f_i,t)h(f_{i+k},t) \qquad k \geq 0. \tag{4.6}$$

where $h(f_i, t)$ is the complex frequency response associated with frequency bin f_i at time t, and N is the number of frequency bins. Figure 4.10 shows the averaged frequency correlation function from the measured data in CASE1. The x-axis is the index of the frequency bin. Thus, the frequency correlation varies with the inter-element spacing and environments. In any of the NLOS scenarios of interest, the frequency correlation coefficient decays along with the number of the frequency bin.

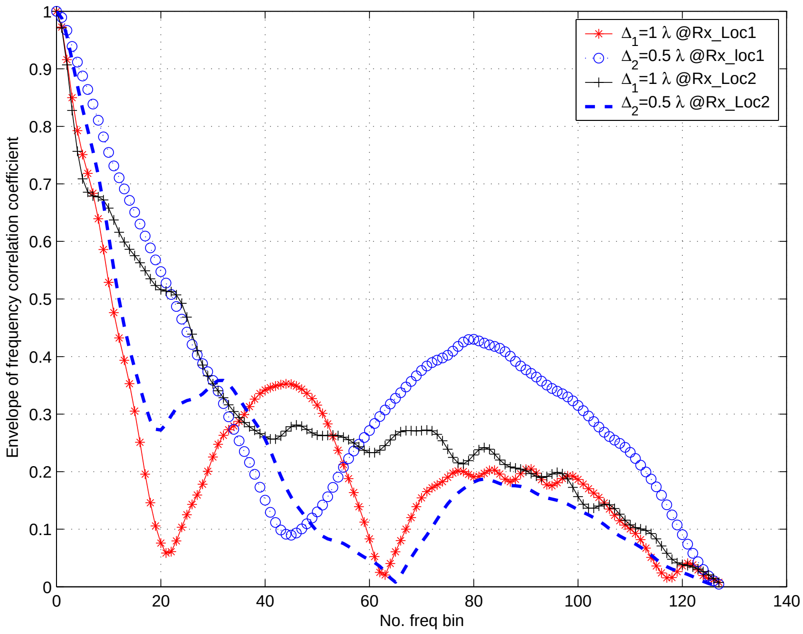

Figure 4.10: Averaged frequency correlation function

4.4 Summary

This chapter describes the characteristics of wideband multipath vector channels and matrix channels for multiple antenna systems in stationary propagation scenarios caused by multipath and array element spacing. Experiments are conducted by using the 1.8 GHz wideband MIMO testbed in outdoor environments with typical LOS and NLOS propagation paths between the transmitter and the receiver. From the measured data, the statistics of the RMS delay spreads in the NLOS environments have been analyzed and the distribution of channel responses based on the elements of the channel matrix is calculated. The results are as follows: (1) The RMS delay spread varies with the environments and intra-element spacing of antennas. When the Rx array is at Rx_Loc1, two or three resolvable multipath clusters are present, and the mean of RMS delay spread is 1.60μs. When the Rx is at Rx_Loc2, the mean of RMS delay spread is 1.55μs. Because significant multipaths exist in the NLOS environments, these channels are treated as frequency-selective or wideband channels. (2) After the FFT of the channel impulse responses, the statistics of matrices via the elements of the channel matrices can be calculated. Here, the frequency response in a frequency bin is extracted and treated as a narrowband channel to obtain the distribution of the magnitude and the phase. The results show that the distribution of magnitude in a frequency bin is close to Rayleigh, and the phase distribution is close to uniform. This result leads to the easy calculation of the wideband channel capacity in the next chapter. (3) Frequency correlation functions are studied based on the measured data in an outdoor NLOS environment. Based on the measured data, the inter frequency correlation decays with increased frequency separation. The above conclusions are based on observations drawn from the wideband matrix channel measurement. We will estimate the channel capacity from the measured data.

Chapter 5

Measured Capacity and MIMO Channel Modeling

5.1 Introduction

In this chapter we study the fundamental limit on the spectral efficiency that can be supported reliably in MIMO wireless channels. The maximum error-free data rate that a channel can support is called the channel capacity [10]. The channel capacity for the additive white Gaussian noise (AWGN) channel was first derived by Claude Shannon in 1948. In contrast to scalar AWGN channels, MIMO channels exhibit various fading and encompass a spatial dimension. The capacity results for MIMO channels have been developed only in the past few years.

MIMO wireless systems use multiple antenna elements at both ends of the transmitter and receiver so as to increase the channel capacity over that of the conventional SISO system. For many years, channels characterized by multipath propagation were considered to be an impairment to wireless communication. However, it has become recently understood that, in a rich scattering environment, multiple antennas can lead to increased channel capacity. A significant amount of research has been directed at determining the MIMO channel capacity [20]. It is also well known that the use of MIMO antenna systems allows the channel capacity to scale in proportion to the minimum number of transmit and receive antennas in uncorrelated Rayleigh fading channels [10]. In such MIMO systems, the spatial diversity of antennas and the radio channel characteristics play a key role in determining the performance of the communication system. For example, the correlation between sub-channels of the matrix channel limits the MIMO channel capacity considerably [53, 54, 55]. In practice, real channels hardly satisfy these ideal assumptions; thus, recent work has focused on measuring and characterizing real MIMO propagation channels.

Research on antenna array configurations and radio channel propagation in MIMO systems has dealt with channel capacity limitation, channel measurements, and modeling. While space-time coding and signal processing are the key to the successful implementation of a MIMO system in the future, considerable research has focused on the propagation channel and antenna design, because these two areas represent major parameters that ultimately impact system performance [32, 33]. For instance, assessing the potential of a MIMO system requires a generalized model for multipath channel characteristics. With the growing interest in implementing MIMO systems, the evaluation of MIMO channel capacity in typical and realistic propagation environments has become important. The goal of this chapter is to study the channel capacity based on the measured data in different NLOS scenarios and to compare the results with the works of other researchers, which include narrowband MIMO measurement [42, 56] and virtual MIMO frequency domain measurement [24, 26].

This chapter is organized as follows. In Section 5.2, we introduce the channel capacity of the MIMO wireless system and extend the capacity from narrowband channel to wideband channel. In Section 5.3, we discuss the channel normalization, and the measured MIMO capacity per frequency bin (narrowband) and over a bandwidth of 2.5 MHz. Section 5.4 compares the measured capacity with the results of other studies. Section 5.5 evaluates the Kronecker MIMO channel model with the measured data. Finally, conclusions are drawn in Section 5.6.

5.2 MIMO Channel Capacity

The wideband channel capacity is the expansion of the capacity of a narrowband channel. Therefore, we first introduce the capacity in the narrowband channel with ideal realizations. Then the wideband channel capacity is discussed.

5.2.1 Capacity of Narrowband MIMO Channel

Consider a MIMO channel with M_T transmit antennas and M_R receive antennas. We assume that the channel is frequency flat over the bandwidth of interest. Denoting the $M_R \times M_T$ channel transfer matrix by $\mathbf{H}$, the input-output relation for the MIMO channel is as follows,

$$\mathbf{r} = \mathbf{H}\mathbf{s} + \mathbf{n} \tag{5.1}$$

where $\mathbf{r}$ is the $M_R \times 1$ received signal vector, $\mathbf{s}$ is the $M_T \times 1$ transmitted signal vector, and $\mathbf{n}$ is the zero mean circularly symmetric complex Gaussian noise with covariance matrix $E(\mathbf{nn}^H) = N_0\mathbf{I}_{M_R}$. The covariance matrix of $\mathbf{s}$, $\mathbf{R_{ss}} = E\{\mathbf{ss}^H\}$, must satisfy $Trace(\mathbf{R_{ss}}) = M_T$ to constrain the total average energy transmitted over a symbol period.

Assume that channel $\mathbf{H}$ is known to the receiver, but is unknown to the transmitter. We can equally allot the total transmit power to each antenna [20]. The capacity C of the MIMO channel in the absence of channel knowledge at the transmitter is given by

$$C = \log_2 \det(\mathbf{I}_{M_R} + \frac{\rho}{M_T}\mathbf{HH}^H) \tag{5.2}$$

where ρ is the signal-to-noise ratio (SNR) and $\mathbf{I}_{M_R}$ is an $M_R \times M_R$ identity matrix.

The use of multiple antennas at the transmitter and receiver in a wireless link opens multiple scalar spatial data pipes (a.k.a. modes) between the transmitter and receiver. For example, if a channel is full-rank with an equal number of transmit and receive antennas ($M_T = M_R = M$), and the elements of $\mathbf{H}$ satisfy $\|\mathbf{H}\|_\mathbf{F}^\mathbf{2} = Trace(\mathbf{HH^H}) = \sum_{i=1}^{M_R}\sum_{j=1}^{M_T} |h_{i,j}|^2 = M^2$, then

$$C = M \log_2(1 + \rho) \tag{5.3}$$

Thus, an orthogonal MIMO channel achieves M times of the SISO channel capacity.

Now consider the capacity of a random MIMO channel with channel matrix $\mathbf{H}$ that is normalized by $E\{|h_{i,j}|^2\} = 1$. When channel information is unknown to the transmitter, each realization of the fading channel has a maximum information rate associated with it. Assuming that $\rho = 20$dB, we compute four sets of antenna configurations through Monte Carlo methods $(M_T = 4, M_R = 4), (M_T = 8, M_R = 4), (M_T = 4, M_R = 8), (M_T = 8, M_R = 8)$ and show the cumulative distribution function (CDF) of information rate in Figure 5.1.

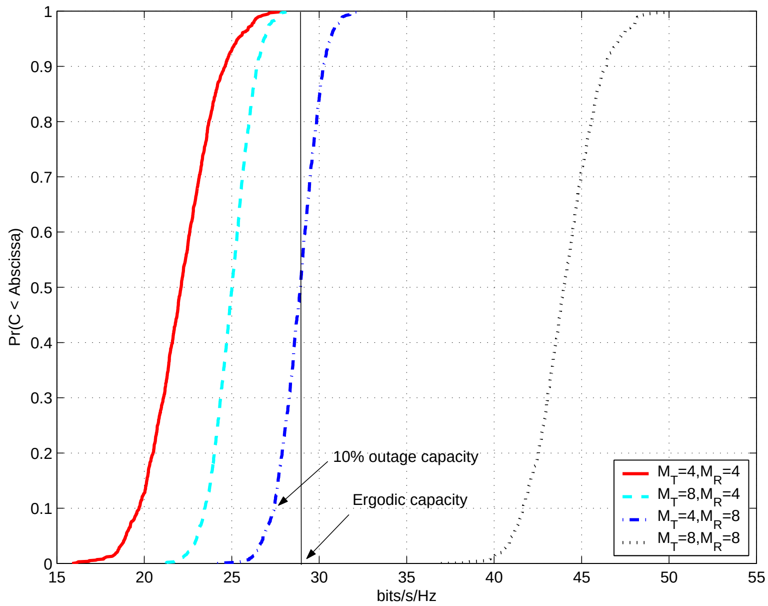

Figure 5.1: CDF of capacity for iid channels

When we analyze the capacity of fading channels, the ergodic capacity and the outage capacity are often used. The ergodic capacity $\overline{C}$ is the ensemble average of the information rate over the distribution of the elements of the channel matrix. For example, when the channel is unknown to the transmitter, the ergodic capacity $\overline{C}$ is defined as

$$\overline{C} = E\{\sum_{i=1}^{k} \log_2(1 + \frac{\rho}{M_T}\lambda_i)\} \tag{5.4}$$

where k is the rank of the channel and $\lambda_i : \ \{i = 1, 2, \cdots, \ k\}$ are the positive eigenvalues of $\mathbf{HH}^H$. In the case of the $(M_T = 4, M_R = 8)$ MIMO system, the ergodic capacity of the iid channel in Figure 5.1 is 28.9 bps/Hz. In contrast, the ergodic capacity of the ($M_T = 8, M_R = 4$) system in the iid channel is 24.9 bps/Hz, less than that of ($M_T = 4, M_R = 8$).

The outage capacity analysis quantifies the level of capacity that is guaranteed with a certain level of reliability. The outage capacity is defined as the capacity that is not achieved with that outage probability. Thus, we define the $q\%$ outage capacity $C_{out,q}$ as the information rate that is guaranteed for $(100 - q)\%$ of the channel realizations, that is, $P(C \leq C_{out,q}) = q\%$ [10]. For example, the 10% outage capacity of ($M_T = 4, M_R = 8$) configuration in Figure 5.1 is 27.3 bps/Hz.

5.2.2 Wideband MIMO Channel Capacity

In wideband MIMO channels, the frequency responses vary in the different environments. Thus, the capacity of a frequency selective fading MIMO channel can be calculated by dividing the bandwidth of interest into N narrower subchannels, each having a bandwidth of $1/N$, such that each subchannel is frequency flat, as shown in Figure 5.2 [57].

If we assume the channel information is unknown to the transmitter and that the transmit power is allocated evenly across transmit antennas and frequency band, the capacity of a deterministic channel can be expressed as [10]:

$$C_{WB} = \frac{1}{N}\sum_{i=1}^{N} \log_2 \det(\mathbf{I}_{M_R} + \frac{\rho}{M_T}\mathbf{H}(f_i)\mathbf{H}^H(f_i))\} \quad (bits/s/Hz) \tag{5.5}$$

where $\mathbf{H}(f_i)$ is the i^{th} subchannel response. If all $\mathbf{H}(f_i)$ have iid property, then, by the strong law of large numbers ($N \longrightarrow \infty$), we can achieve the capacity of the frequency selective channels.

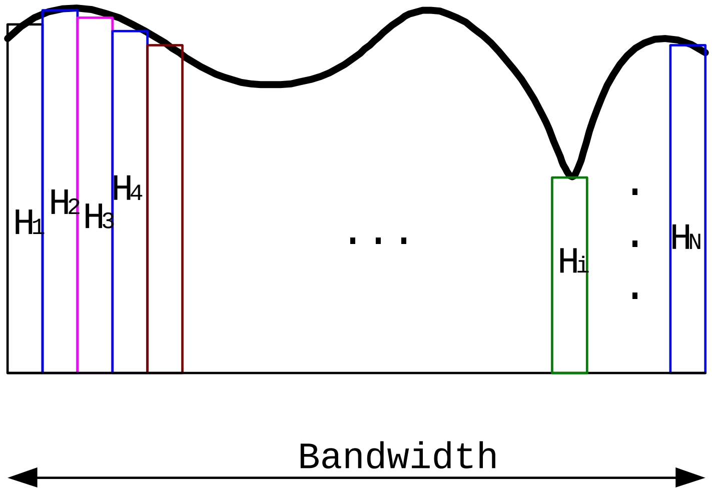

Figure 5.2: Wideband channel capacity is the sum of the capacity of frequency flat bins

5.3 Measured Capacity of NLOS Channels

In this section, we use the measured data in Case Study 1 to compute the channel capacity. The experimental setup consists of four different combinations of array and scenes, that is, two different NLOS environments and two different intra-element spacings of the Rx antenna array. We first show the measured capacity in a frequency bin (narrowband) and then compare it with the capacity from the narrowband iid simulation. We proceed to the measured capacity in the wideband NLOS channels and show the differences with iid simulations.

5.3.1 Normalization of MIMO Channel Responses

Since the actual received signal strength varies with the Tx and Rx locations, channel normalization is necessary to facilitate a comparison of capacities at different locations. The normalization factor for each wideband measurement snapshot is calculated independently. This approach removes the effect of large-scale spatial fading, which can significantly affect the dynamic range of received signals, and ensures that only small-scale fading is considered. One reasonable normalization is to scale the channel matrix such that the average power transfer between a Tx and a Rx antenna is unity, as suggested in [58]. Let $\mathbf{H}(f_i)$ and $\hat{\mathbf{H}}(f_i)$ represent the measured and normalized matrices, respectively. N is the number of frequency subband in Figure 5.2. Here we apply the Frobenius norm to normalize $\mathbf{H}(f_i)$ as follows:

$$\hat{\mathbf{H}}(f_i) = \mathbf{H}(f_i) \times \left(\frac{1}{N M_T M_R} \sum_{f_i=1}^{N} \|\mathbf{H}(f_i)\|_F^2 \right)^{-\frac{1}{2}} \tag{5.6}$$

and $\hat{\mathbf{H}}(f_i)$ is used in place of $\mathbf{H}(f_i)$ in Equation 5.5 for calculating the measured channel capacity.

5.3.2 Measured Capacity In a Frequency Bin

The eigenvalues from the channel matrices play a very important role in channel capacity. By examining the eigenvalues, we can select a set of measured data of the 4×8 system with an Rx intra-element spacing of 1λ and at the Rx_Loc2 site. Because the bandwidth of our channel sounder is 2.5 MHz, we divide the whole bandwidth into $N = 128$ frequency bin. Thus, each frequency bin is 2.5 MHz/128=19.53 kHz, and we treat the channel responses as flat in this narrowband frequency bin. Figure 5.3 shows the comparison of the eigenvalues of $\mathbf{H}\mathbf{H}^H$ in a typical frequency bin (a) and the eigenvalues of iid simulation (b).

In Figure 5.3, the averaged eigenvalues are calculated over location and

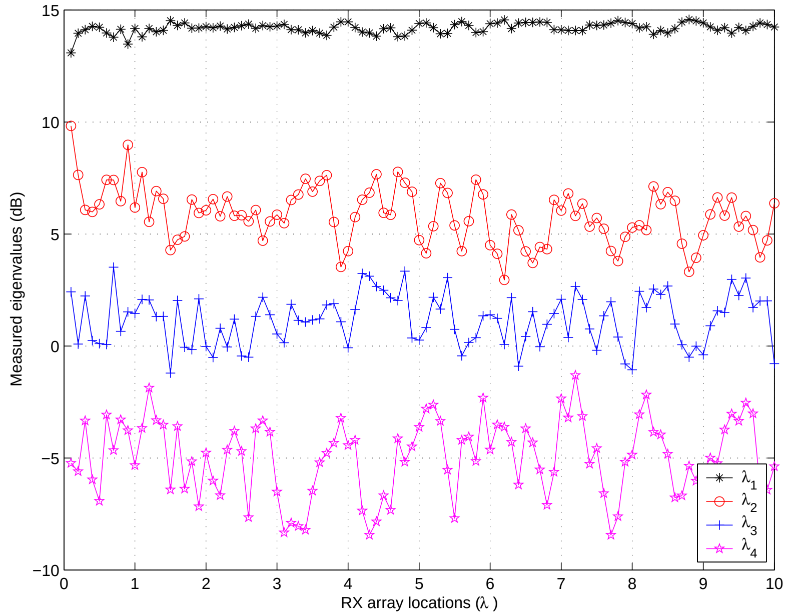

(a) Measured eigenvalues

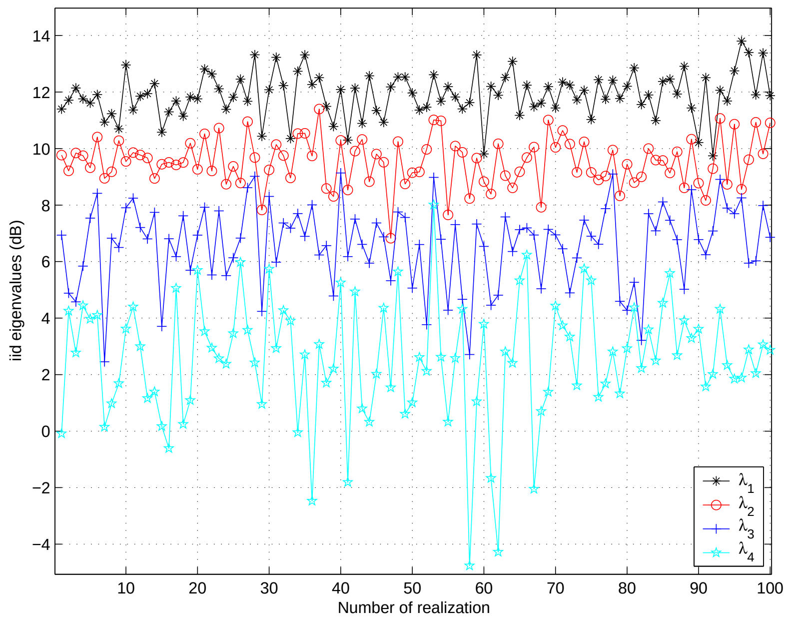

(b) The iid simulated eigenvalues

Figure 5.3: Eigenvalue comparisons. (a) Measured eigenvalues. (b) The iid simulated eigenvalues

frequency bin. Because there are 36 channel realizations at one location, the averaged eigenvalues become smooth over 100 locations or 10 wavelengths (for simplicity, we chose 100 instead of 101 locations). The second eigenvalue λ_2 fluctuates and is around 8 dB less than the largest eigenvalue λ_1. Compared with the simulation from the independently and identically distributed (iid) channels in Figure 5.3(b), the first measured λ_1 is larger and smoother than the iid eigenvalue. The rest of the eigenvalues, however, are smaller than those of the iid simulation. This difference is the effect of normalization, which preserves the same transmission powers for both the measured channel responses and the iid simulation. Therefore, the measured eigenvalues show less diversity than the iid simulation, and the measured capacity is also smaller than the iid capacity. This fact is shown in Figure 5.4 by the CDF of capacity. As always, the signal-to-noise ratio is assumed to be 20 dB .

Because the antennas are considered as the measurement environment, we extract different sizes of subarrays, for example, 2×2, 3×3, and 4×4 arrays, and compare these smaller MIMO systems with the ideal simulation. To compare the narrowband results with previous findings [42], the SNR ρ is set to 10 dB. Figure 5.5 shows the comparisons of the measured capacity with iid channel capacity in terms of outage analysis for ρ =10 dB. In [42], Chizhik et al. measured the narrowband MIMO channel capacity in Manhattan and found that the median capacity of the 4×4 and 16×16 systems were 90% and 78%, respectively, of the corresponding capacities of the complex Gaussian iid channel. The capacity results in our measurement show we can achieve 92% and 85% of median capacity of the iid capacity for 3×3 and 4×4 systems, respectively. Note that although the median capacity percentages are similar, a one-to-one comparison is not possible because of the differences in the system

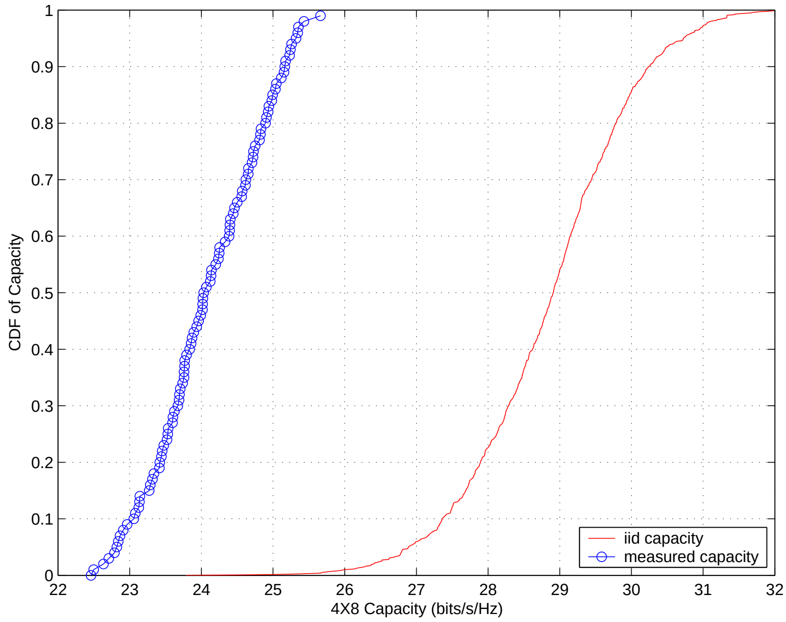

Figure 5.4: The measured capacity vs. Rayleigh iid (assume a 4 x 8 system and ρ =20 dB).

sizes.

Observe that, for the MIMO channels in a frequency bin, the cumulative density function of the measured capacity becomes steeper than the corresponding Rayleigh channel capacity with the same array sizes. When the array size increases, the difference in the outage capacity at the 50% percentile increases quickly. For example, given the array size of 2×2, the difference of the outage capacity is 0.1 bps/Hz. In the case of an array size of 3×3, the difference of the outage capacity is 0.7 bps/Hz. For an array size of 4×4, the difference of the outage capacity is 1.5 bps/Hz.

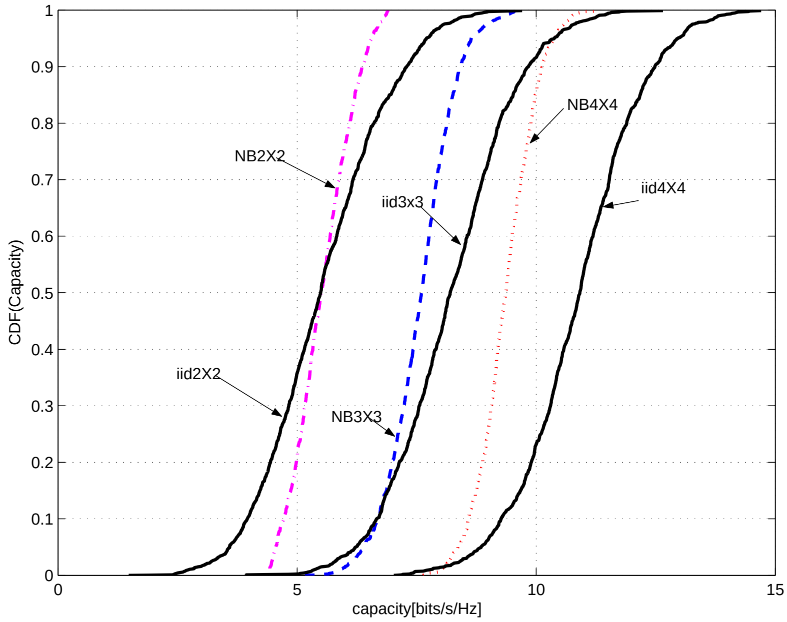

Figure 5.5: Capacity distribution of the measured narrowband (NB) vs. iid channels (assume ρ =10 dB and array sizes $M_T = M_R = 2, 3, 4$).

5.3.3 Measured Wideband MIMO Capacity

Field measurements were conducted by the wideband true array channel sounder with four transmit antennas and eight receive antennas. After the channel data collections described in Chapter 4, we first extract the channel impulse responses, and then use a Fourier transform to calculate the channel frequency responses. Based on the channel frequency responses, we already recognize that the channel of NLOS environments is frequency selective or is wideband. The wideband MIMO channel capacity is then computed based on Equation 5.5. Our experiments were conducted based on the Rx locations at two different NLOS environments. Thus, the channel capacity can be associated with many factors, such as Rx array inter-element spacing, environment, Rx locations, and so on.

Case Study 1: This experimental setup was described in Chapter 4. The Tx antenna array is fixed on the roof of the EERL building, and the Rx antenna is located at Rx_Loc1. Channel data are collected based on the locations of the Rx antenna array. A total of $303 \times 12 = 3636$ channel matrices (8 by 4) are recorded. The average capacity over three snapshots of measurement and 12 channel samples per snapshot is taken at each location.

Figure 5.6(a) shows the capacity in a bandwidth of 2.5 MHz associated with the Rx array locations. Note that the channel capacity fluctuates with the Rx locations. In this non-line-of-sight environment, the channel responses change dramatically even for small displacements of the Rx array because of the structure of the multipath. Therefore, the wideband capacity is a function of the location of the Rx antenna array. Figure 5.6(b) shows the CDF of the measured capacity and the ideal channel capacity. Observe also that, for a 4×8 MIMO system with a 2.5 MHz bandwidth and at 10% outage probability, one 2.5 MHz channel can provide a capacity of 46 Mbps and 48 Mbps, respectively, for an Rx array with intra-element spacing of $\Delta_1 = 0.5\lambda$ and $\Delta_2 = 1\lambda$. Moreover, the achieved capacity is approximately 70% of the theoretical capacity with the same bandwidth.

Case Study 2: This experimental setup was described in Chapter 4. The Tx antenna is fixed on the roof of the EERL Building, and the Rx antenna is located at Rx_Loc2. Channel data are collected based on the locations of the Rx antenna array. A total of $303 \times 12 = 3636$ channel matrices are recorded. The average capacity over three snapshots and 12 channel responses per snapshot is taken at each location.

Figure 5.7(a) shows the capacity in a bandwidth of 2.5 MHz associated with the Rx array locations. Note that the channel capacity fluctuates with the

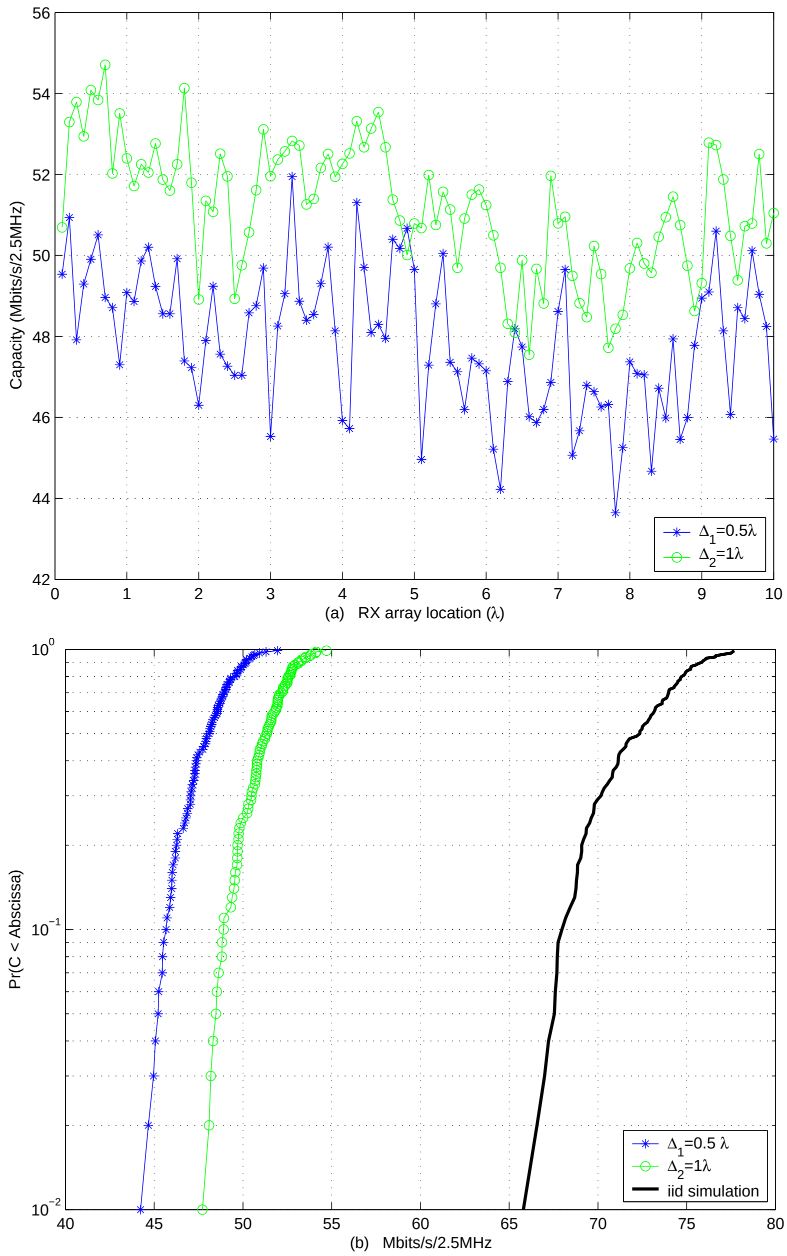

Figure 5.6: Measured wideband 4×8 MIMO channel capacity. Rx array is set up at Rx_Loc1. (a) Capacity calculated based on locations. (b) CDF of capacity vs. iid theoretical results

Rx locations. Therefore, the wideband capacity is a function of the location of the Rx antenna array. Figure 5.7(b) shows the CDF of the measured capacity and the ideal channel capacity. Observe that, for a 4 x 8 MIMO system with a 2.5 MHz bandwidth and a 10% outage probability, one 2.5 MHz channel can provide a capacity of 56.2 Mbps and 62.7 Mbps, respectively, for an Rx array with intra-element spacing of $\Delta_1 = 0.5\lambda$ and $\Delta_2 = 1\lambda$. Moreover, the achieved capacity is around 80% $\sim$ 90% of theoretical capacity with the same bandwidth. These results show that, even though an identical setup is used, the measured CDF capacities can differ from each other if the measurements are taken in different environments.

To compare the wideband capacity with the narrowband capacity, we extract the data contained in subarrays, that is, 2×2, 3×3, and 4×4. For easy comparison, the wideband capacity is normalized to unit bandwidth. To compare the wideband results with previous findings [25], the SNR ρ is set to 10 dB. Figure 5.8 shows the comparisons of the measured wideband capacity with the narrowband channel capacity in the terms of outage analysis for ρ =10 dB. Molisch et al. in [25] shows that the outage capacity approaches the mean capacity as the bandwidth increases from narrowband to a bandwidth of 100 MHz for array sizes $M_T = M_R = 1, 2, 4, 8$. Our wideband channel measurement shows that the CDF capacity becomes steeper than the narrowband CDF capacity for subarrays $M_T = M_R = 2, 3, 4$. However, a one-to-one comparison is not possible because of differences in the system array and bandwidth.

Observe that, for the wideband MIMO channels, the cumulative density function of the measured capacity becomes steeper than the corresponding narrowband channel capacity with the same array sizes. This change is to be expected because the frequency selectivity of the channel adds additional

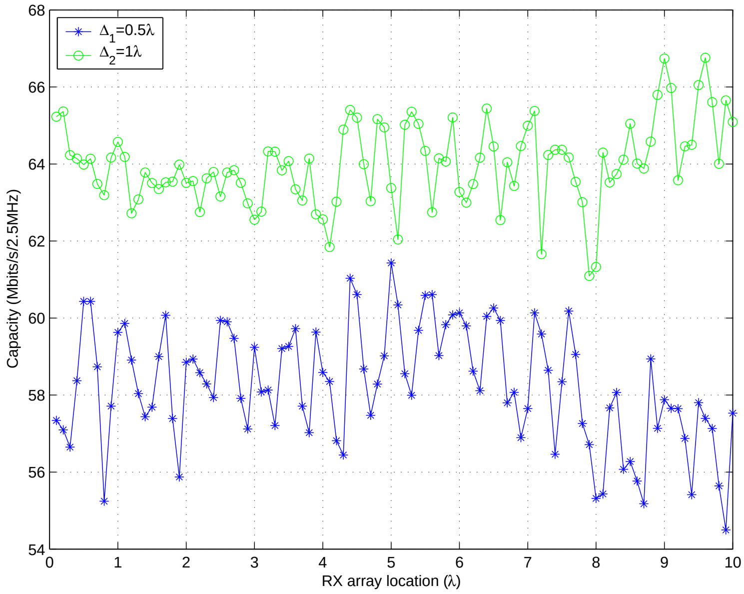

(a) Capacity calculated based on locations.

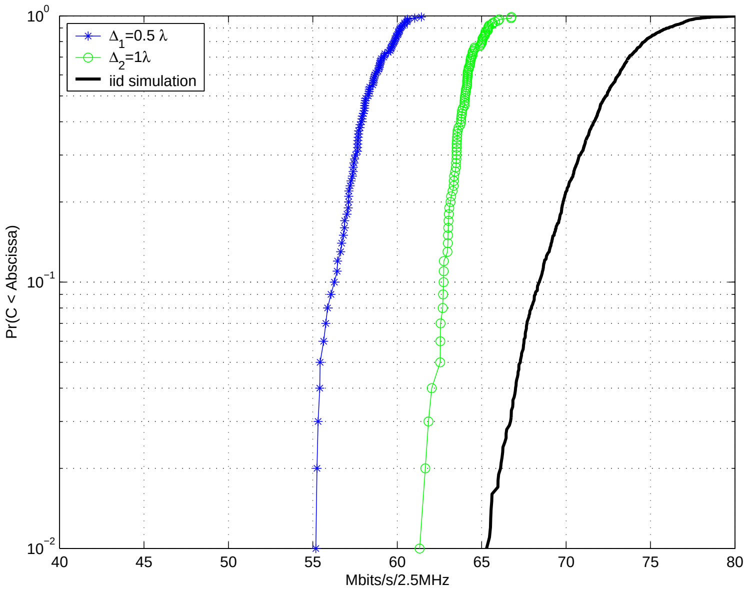

(b) CDF of capacity vs. iid theoretical results

Figure 5.7: Measured wideband 4×8 MIMO channel capacity. Rx array is set up at Rx_Loc2. (a) Capacity calculated based on locations. (b) CDF of capacity vs. iid theoretical results

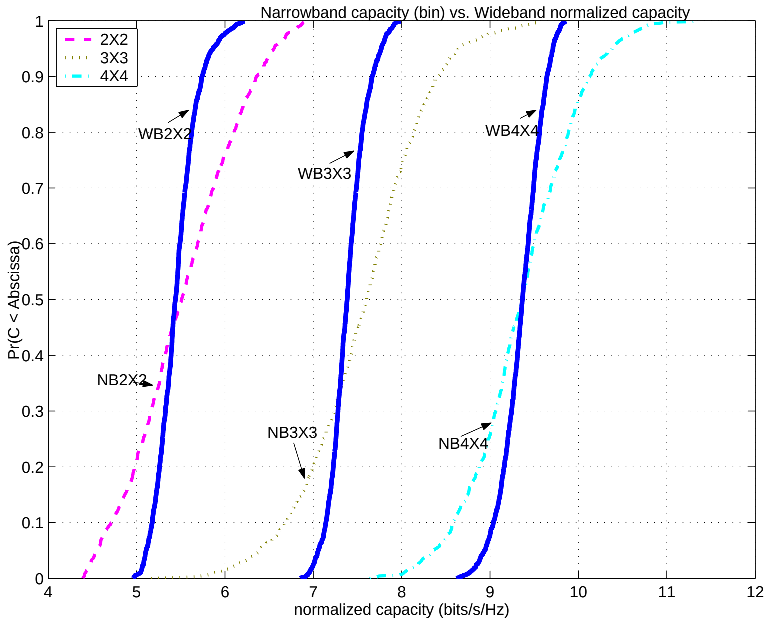

Figure 5.8: Comparisons of CDF capacity of narrowband vs. normalized wideband. Assume ρ =10 dB for array sizes $M_T = M_R = 2, 3, 4$.

diversity, so that the outage capacity comes closer to the mean capacity.

5.4 Comparisons With Existing MIMO Measurement Results

The MIMO channel capacity is the major parameter for showing the characteristics of a radio channel. Researchers have developed many ways to obtain the MIMO channel impulse responses [20, 26, 42]. Based on the measured responses, a quick comparison of the MIMO channel capacities under different environments can be performed. Because the channel capacity in a frequency bin can be treated as a narrowband capacity, the capacity comparison begins with the work done by Chizhik et al. [42]. The channel measurements were carried out in Manhattan with a 16×16 narrowband MIMO testbed, and the carrier frequency was 2.11 GHz. The results showed high capacities within 80% of the fully scattering channel capacity. It was reported that another 4×4 median system capacity in suburban New Jersey reached 68% of the corresponding capacity of the complex Gaussian iid channel. In Figure 5.4, which depicts the CDF capacity of a 4×8 system, we can achieve the median capacity around 24(bps/Hz)/29(bps/Hz) = 82.76% of the iid capacity, which is a little more than that in Chizhik's work. The reason for the difference may be that the frequency bin selected had better scattering and may have had small frequency diversity.

Regarding wideband channel capacity, the measured results were compared with the findings of Molisch et al. [25]. In that paper, the authors used a virtual MIMO channel sounder based on the frequency swept technique. The operating frequency was 5.2 GHz with a bandwidth of 10 MHz or 100 MHz. The authors found the capacities to be about 30% smaller than would be anticipated from an idealized model. In the capacity results, we obtained a higher percentage (more than 70%) of the ideal capacity than the counterpart, given the same ρ=10 dB. However, the influences, such as the carrier frequency, mutual coupling effects, environment, and measurement technique, had to be neglected. Therefore, it does not really make sense to compare one MIMO system to another MIMO system with data taken in different environments. Thus, we really need to compare how well the data compares with model predictions.

When we try to compare the characteristics of two MIMO channels, a standard for the parameters should be established. Obviously, the simplest way is to compare the MIMO channel capacity. The higher the capacity, the better, and the easier it is to design the communication system. In fact, however, such a comparison is not adequate. Since the channel capacity is derived from the channel responses, which are environment-dependent (even after **H** normalization), the capacity is strongly dependent on the environment. Thus, we need to develop a good channel model for this kind of comparison.

Currently, there are many different MIMO channels, such as the Kronecker model, the Weichselberger model, and the virtual channel representation [26, 59, 60]. Yet, no single model is perfect, and no unified MIMO channel model covers all the radio channel characteristics. It is difficult, therefore, to compare MIMO channels directly. Ideally, if there exists a MIMO channel model, into which one inputs the main channel characteristics obtained from measurements, that model can output the channel impulse responses that can statistically substitute for the original measured **H**. If that were the case, we could say we had a universally valid MIMO channel model. Then, we could compare the measured channel responses with the modeling results.

5.5 MIMO Channel Modeling With Measured Data

Channel modeling for MIMO links in a multi-path scattering environment is a key issue for future MIMO systems, because most realistic channels are spatially correlated as opposed to the idealized iid model. The popular Kronecker model assumes separation in the transmit and receive statistics, which imposes strong conditions on the degrees of freedom and diversity of the MIMO channel. Some experiments on real data that show the effectiveness of these models in realistic environments are presented in [26, 61]. In this section, we study the Kronecker MIMO channel model by using the measured data in NLOS environments.

5.5.1 Kronecker MIMO Channel Model Investigation

Let us start from the flat-fading channel model defined in Equation 5.1. We will describe the general spatial correlation functions and then derive a discrete expression of the spatial correlation used for the measured data. As previously mentioned, we usually normalize $\mathbf{H}$ for all the measured channel realizations such that $E[\|\mathbf{H}\|_F^2] = M_T M_R$, where $E[.]$ denotes the expected value, which averages over all measured channel realizations for a specific link.

In [53], the spatial fading correlation for a narrowband flat-fading MIMO channel $\mathbf{H}$ is defined as

$$\mathbf{R}_H = E[vec(\mathbf{H})vec(\mathbf{H})^H] \tag{5.7}$$

where $vec(\mathbf{H})$ denotes the $M_R M_T \times 1$ vector composed of stacking the columns of $\mathbf{H}$ and $(.)^H$ denotes a Hermitian transpose. In a rich scattering environment, the spatial correlation between the transmit antennas ($\mathbf{R}_{Tx}$) can be assumed to be independent from the correlation between the receive antennas ($\mathbf{R}_{Rx}$) [43]; therefore, $\mathbf{R}_H$ can be written as

$$\begin{aligned}\mathbf{R}_H &= \mathbf{R}_{Tx}^T \bigotimes \mathbf{R}_{Rx} \\ &= \begin{bmatrix} (\mathbf{R}_{Tx}^T)_{11}\mathbf{R}_{Rx} & \cdots & (\mathbf{R}_{Tx}^T)_{1M_T}\mathbf{R}_{Rx} \\ \vdots & \ddots & \vdots \\ (\mathbf{R}_{Tx}^T)_{M_T1}\mathbf{R}_{Rx} & \cdots & (\mathbf{R}_{Tx}^T)_{M_TM_T}\mathbf{R}_{Rx} \end{bmatrix}\end{aligned} \tag{5.8}$$

with $\bigotimes$ denoting the Kronecker product [62], $(.)^T$ stands for the transpose of the corresponding matrix, and $\mathbf{R}_{Tx}$ and $\mathbf{R}_{Rx}$ are defined as

$$\mathbf{R}_{Tx} = E\{[(\mathbf{h}^i)^H \mathbf{h}^i]^T\}, \quad i = 1,\ 2,\ \cdots,\ M_R \tag{5.9}$$

$$\mathbf{R}_{Rx} = E[\mathbf{h}_j (\mathbf{h}_j)^H], \quad j = 1,\ 2,\ \cdots,\ M_T \tag{5.10}$$

where $\mathbf{h}^i$ is the i^{th} row of $\mathbf{H}$, and $\mathbf{h}_j$ is the j^{th} column of $\mathbf{H}$. To generate independent narrowband flat-fading MIMO channel realization with spatial correlation, the following expression can be used [61]:

$$\mathbf{H} = reshape(\mathbf{R}_H^{\frac{1}{2}} \mathbf{g}) \tag{5.11}$$

where $\mathbf{g}$ is an $M_R M_T \times 1$ stochastic vector with iid zero-mean unit variance complex Gaussian elements, and $reshape(.)$ is the reverse of the $vec(.)$ operation. By using some special properties of $\mathbf{R}_H$ and a Kronecker product identity, we can write Equation 5.11 in a more commonly used form. Note that $\mathbf{R}_H$ is Hermitian and nonnegative definite. Hence, we may apply eigenvalue decomposition, as in [62]:

$$\begin{aligned} \mathbf{R}_H &= \mathbf{U} \mathbf{\Lambda}_H \mathbf{U}^H \\ &= \mathbf{U} \mathbf{\Lambda}_H^{\frac{1}{2}} \mathbf{\Lambda}_H^{\frac{1}{2}} \mathbf{U}^H \\ &= (\mathbf{U} \mathbf{\Lambda}_H^{\frac{1}{2}})(\mathbf{U} \mathbf{\Lambda}_H^{\frac{1}{2}})^H \\ &= \mathbf{R}_H^{\frac{1}{2}} (\mathbf{R}_H^{\frac{1}{2}})^H \end{aligned} \tag{5.12}$$

from which we obtain the square-root of $\mathbf{R}_H$. Such decompositions also hold for $\mathbf{R}_{Tx}$ and $\mathbf{R}_{Rx}$. Consequently, from Equation 5.8, it follows that

$$\begin{aligned} \mathbf{R}_H &= \mathbf{R}_{Tx}^T \bigotimes \mathbf{R}_{Rx} \\ &= [\mathbf{R}_{Tx}^{\frac{1}{2}} (\mathbf{R}_{Tx}^{\frac{1}{2}})^H]^T \bigotimes [\mathbf{R}_{Rx}^{\frac{1}{2}} (\mathbf{R}_{Rx}^{\frac{1}{2}})^H] \\ &= [(\mathbf{R}_{Tx}^{\frac{1}{2}})^* \bigotimes (\mathbf{R}_{Rx}^{\frac{1}{2}})][(\mathbf{R}_{Tx}^{\frac{1}{2}})^* \bigotimes (\mathbf{R}_{Rx}^{\frac{1}{2}})]^H \\ &= \mathbf{R}_H^{\frac{1}{2}} (\mathbf{R}_H^{\frac{1}{2}})^H \end{aligned} \tag{5.13}$$

where superscript $*$ denotes the point-wise conjugation. For any matrix $\mathbf{A}$, $\mathbf{B}$, $\mathbf{C}$, and $\mathbf{D}$ with proper dimensions, we have $(\mathbf{AB})\bigotimes(\mathbf{CD}) = (\mathbf{A}\bigotimes\mathbf{C})(\mathbf{B}\bigotimes\mathbf{D})$. Based on the Kronecker product identity that for any matrix with proper dimension there exists $vec(\mathbf{ABC}) = (\mathbf{C}^T\bigotimes\mathbf{A})vec(\mathbf{B})$, then Equation 5.11 can be rewritten as

$$\begin{aligned}
\mathbf{H} &= reshape(\mathbf{R}_H^{\frac{1}{2}}\mathbf{g}) \\
&= reshape\{[(\mathbf{R}_{Tx}^{\frac{1}{2}})^H]^T\bigotimes\mathbf{R}_{Rx}^{\frac{1}{2}}vec(\mathbf{G})\} \\
&= \mathbf{R}_{Rx}^{\frac{1}{2}}\mathbf{G}(\mathbf{R}_{Tx}^{\frac{1}{2}})^T
\end{aligned} \tag{5.14}$$

where $\mathbf{G} = reshape(\mathbf{g})$ is a stochastic $M_R \times M_T$ matrix with iid complex Gaussian zero-mean unit variance elements. Therefore, given a complex Gaussian channel and the Kronecker structure of MIMO channel covariance matrix in Equation 5.8, the MIMO channel matrix can be modeled as in Equation 5.14. This is the Kronecker model [43, 54].

When system simulation needs to be carried out, one way to proceed is to explicitly state the specific correlation matrices $\mathbf{R_{Tx}}$ and $\mathbf{R_{Rx}}$ covering the various propagation scenarios. To obtain these specific correlation matrices, we have to perform either ray tracing or correlation measurements for different scenarios.

5.5.2 Evaluation of the Kronecker MIMO Channel Model

We choose the MIMO channel responses in a frequency bin (narrowband) to evaluate the Kronecker model. From Equations 5.8, 5.9, and 5.10, the transmitter, receiver, and channel covariance matrices are estimated by the corresponding measured channel responses, given as

$$\hat{\mathbf{R}}_{Tx} = \frac{1}{M_R N}\sum_{n=1}^{N}\sum_{i=1}^{M_R}[(\hat{\mathbf{h}}^i)^H\hat{\mathbf{h}}^i]^T \tag{5.15}$$

$$\hat{\mathbf{R}}_{Rx} = \frac{1}{M_T N} \sum_{n=1}^{N} \sum_{j=1}^{M_T} [\hat{\mathbf{h}}_j \hat{\mathbf{h}}_j^H] \tag{5.16}$$

$$\hat{\mathbf{R}}_H = \frac{1}{N} \sum_{n=1}^{N} [vec(\hat{\mathbf{H}}) vec(\hat{\mathbf{H}})^H] \tag{5.17}$$

where N is the number of channel matrices obtained from measurements. $\hat{\mathbf{H}}$ is the measured channel matrix realization, $\hat{\mathbf{h}}^i$ is the i^{th} row of $\hat{\mathbf{H}}$, and $\hat{\mathbf{h}}_j$ is the j^{th} column of $\hat{\mathbf{H}}$. The notation ($\hat{\cdot}$) is used to denote a sample estimate.

We extract the measured data for a subarray 2×2 MIMO system and calculate the covariance based on Equations 5.15, 5.16, and 5.17. The following are the results.

$$\hat{\mathbf{R}}_{Tx} = \begin{bmatrix} 0.9825 & 0.2954 - 0.6629i \\ 0.2954 + 0.6629i & 1.0338 \end{bmatrix} \tag{5.18}$$

$$\hat{\mathbf{R}}_{Rx} = \begin{bmatrix} 0.9966 & -0.3348 + 0.4091i \\ -0.3348 - 0.4091i & 1.0655 \end{bmatrix} \tag{5.19}$$

$$\hat{\mathbf{R}}_H = \begin{bmatrix} 0.9897 & -0.3944 + 0.3978i & 0.0864 + 0.6634i & -0.4375 - 0.0946i \\ -0.3944 - 0.3978i & 1.0396 & 0.5262 - 0.4691i & 0.5582 + 0.4952i \\ 0.0864 - 0.6634i & 0.5262 + 0.4691i & 1.0461 & 0.0314 + 0.4550i \\ -0.4375 + 0.0946i & 0.5582 - 0.4952i & 0.0314 - 0.4550i & 0.9246 \end{bmatrix} \tag{5.20}$$

Note that the correlation at the receiver side is different from that at the transmitter side, although we chose the data from intra-element spacing of 1λ for both the Rx and Tx array in Case Study 1. Based on the covariance matrices at both ends, we can generate the iid channel and model the 2 x 2 system. The cumulative distribution functions of the narrowband capacity for the measured data, the Kronecker model, and the iid MIMO channel are shown in Figure 5.9. Observe that the modeled curve is close to the measured curve.

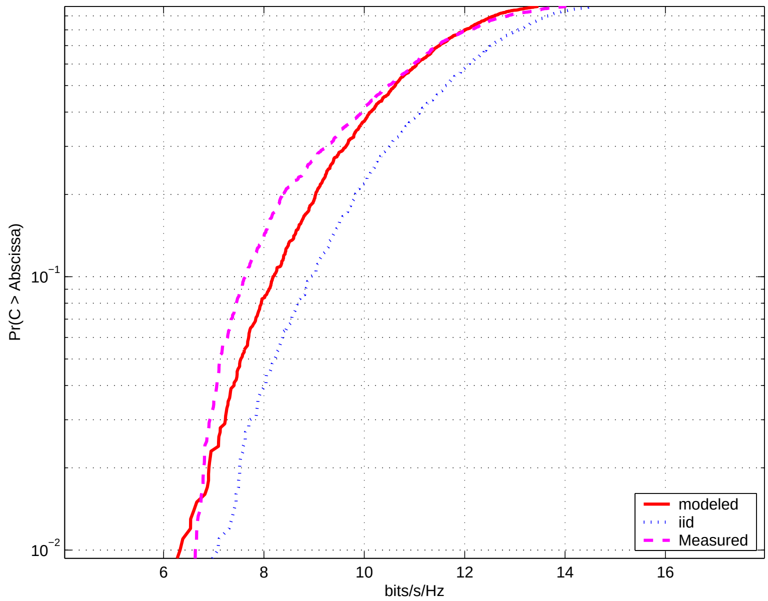

Figure 5.9: CDF of narrowband capacity for measured data, the Kronecker model, and the iid MIMO channel. 2×2 system, ρ =20 dB

Both the cumulative distribution functions of the modeled and the measured capacity cannot reach the iid value given the same outage probability.

Next we evaluate the 3 x 3 system by the Kronecker model. Since the covariance matrices become bigger, we do not show those complex values in detail here. However, the cumulative distribution functions of the capacity by the Kronecker model, the measured data, and the iid are shown in Figure 5.10. Observe that, given the same outage probability, the measured capacity is always larger than the modeled capacity. The difference of the median capacity between the modeled data and measured data is about 0.8 bps/Hz.

Next we present the cumulative distribution functions of the capacity of

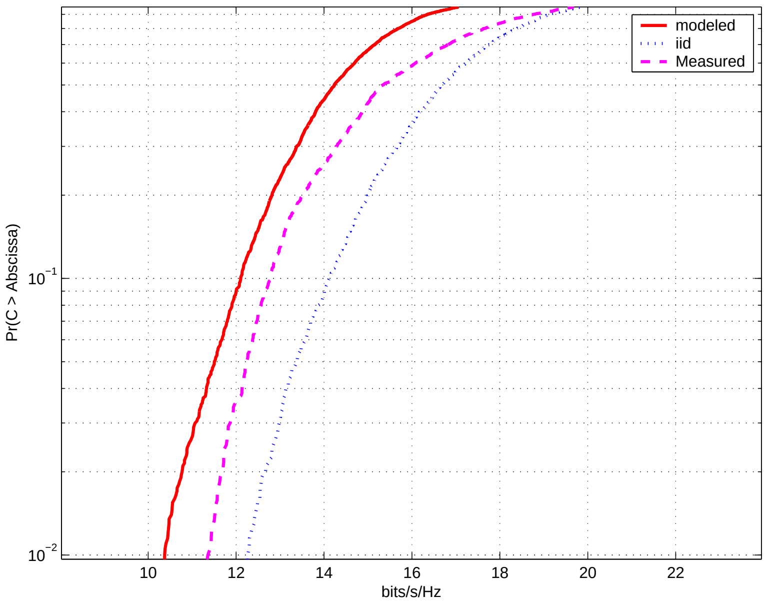

Figure 5.10: CDF of narrowband capacity for measured data, the Kronecker model, and the iid MIMO channel. 3×3 system, ρ =20 dB

a 4 x 4 system by the Kronecker model, the measured data, and the iid, which are shown in Figure 5.11. The same observation applies as for the above 3 x 3 system. At a given outage probability, the measured capacity is always larger than the modeled capacity. The difference of the median capacity between the modeled data and measured data is about 2.8 bps/Hz, larger than the difference in the 3 x 3 system.

Finally, we show the cumulative distribution functions of the capacity in the 4 x 8 system by the Kronecker model, the measured data, and the iid, which are shown in Figure 5.12. Notice that, at a given outage probability, the measured capacity is also always larger than the modeled capacity. The difference of the median capacity between the modeled data and measured data is about 2.8 bps/Hz, the same as for the 4 x 4 system.

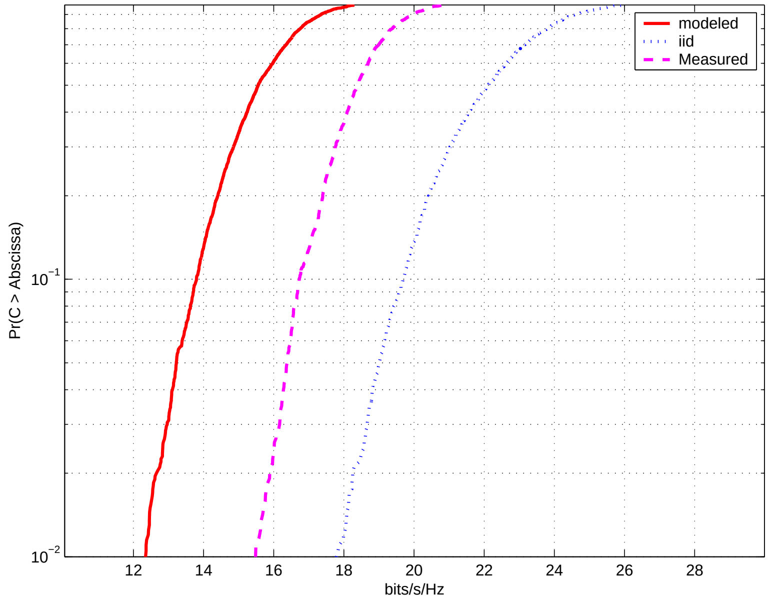

Figure 5.11: CDF of narrowband capacity for measured data, the Kronecker model, and the iid MIMO channel. 4×4 system, $\rho =$20 dB

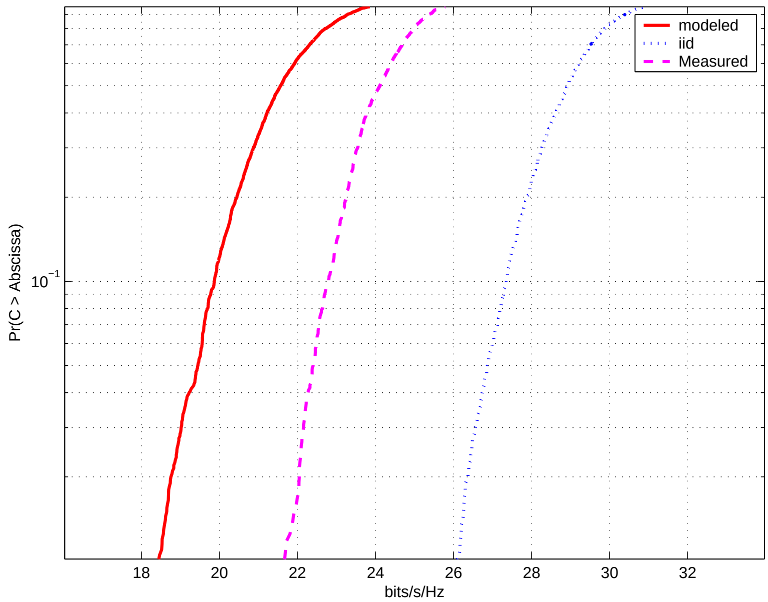

Figure 5.12: CDF of narrowband capacity for measured data, the Kronecker model, and the iid MIMO channel. 4×8 system, $\rho =$20dB

Thus, we conclude that with the increase of array size, the error of the Kronecker model becomes serious, at least from the point of view of the CDF capacity. In other words, this model may have some defects for covering larger array sizes or a considerably correlated MIMO system [63].

5.5.3 Eigenvalue Analysis of the Kronecker Model

One of the most important parameters in a MIMO channel is the eigenvalue distribution of the channel matrix. The spread of the channel matrix eigenvalue is a measure of the orthogonality of the MIMO channel. A large eigenvalue spread means that the channel matrix is highly non-orthogonal and vice versa. Orthogonal channels are desirable since more information is provided [10]. Consider the ideal Rayleigh channels of a 4×8 system with the distribution of the eigenvalues $\lambda_1, \lambda_2, \lambda_3$, and λ_4 shown in Figure 5.13. This result is derived from the Monte Carlo simulation by running 2000 channel realizations. Notice that the four eigenvalues are spread evenly on a dB scale, and each follows a normal distribution.

Figure 5.14 shows the eigenvalue distribution from the Kronecker model by running 2000 channel realizations. Compared with Figure 5.13, the distribution of the biggest eigenvalue is separated from the other eigenvalues. Three small eigenvalues are attenuated, so as to keep the characterization of channel normalization.

Figure 5.15 shows the eigenvalue distribution from the measured data in a frequency bin. Compared with Figure 5.13, the distribution of the biggest eigenvalue is isolated from the other eigenvalues. Three small eigenvalues are attenuated so as to keep the characterization of channel normalization. By

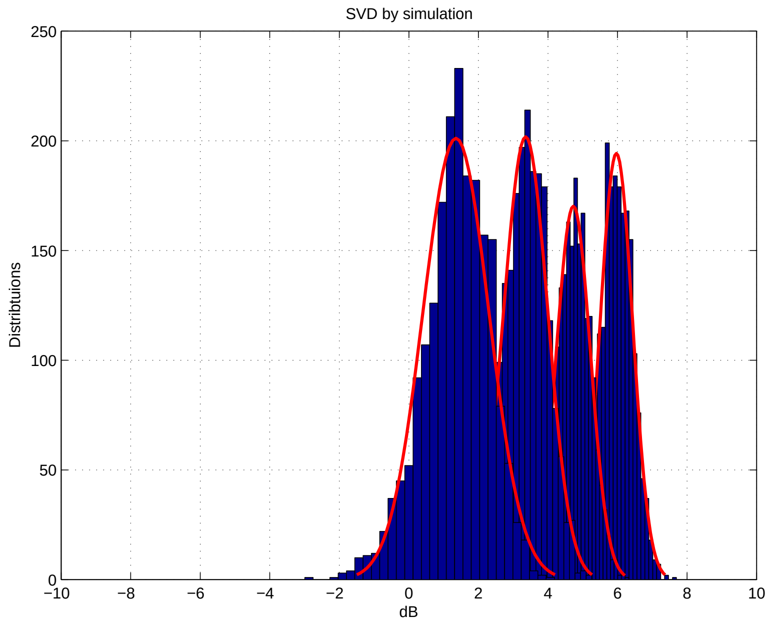

Figure 5.13: Eigenvalue distribution of the iid MIMO channel. 4×8 system

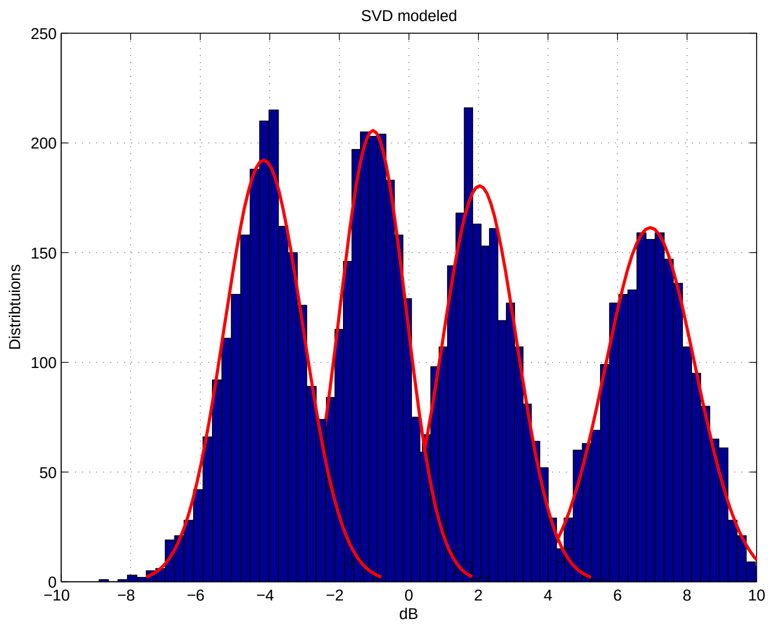

Figure 5.14: Eigenvalue distribution of the Kronecker MIMO channel. 4×8 system

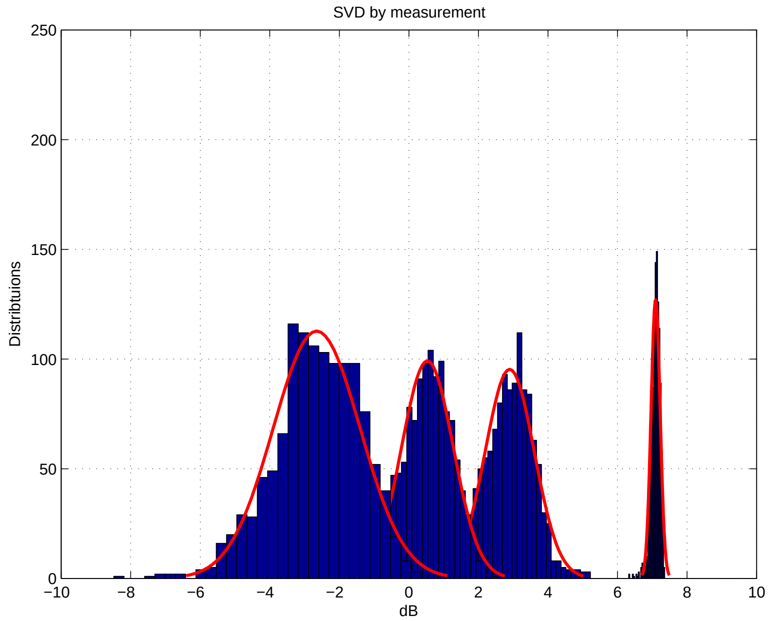

Figure 5.15: Eigenvalue distribution of the measured MIMO channel. 4×8 system

analyzing the differences between the eigenvalue distributions in the 4×8 system, it is shown that the Kronecker model cannot capture all features of the MIMO channel.

5.6 Summary

This chapter has presented the measured capacities in a frequency bin (narrowband) and in the wideband channels with a bandwidth of 2.5 MHz. The measured capacity can achieved more than 70% of the theoretical capacity in non-line-of-sight environments with the 4 x 8 MIMO system. It is found that the outage capacity of a wideband channel is higher than the outage capacity of a narrowband channel at low outage rates. This difference is attributed to the increased tightening of the CDF of capacity due to frequency diversity. The second part in this chapter compares our measured capacity with measurement results from other studies and evaluates the Kronecker MIMO model by our measured data under different array sizes. It is found that, with the increase of array size, the model error of Kronecker model becomes serious, at least from the point of view of CDF capacity. In other words, this model may have some defects in covering larger array sizes or considerably correlated MIMO systems. The Kronecker model overestimates the correlation of transmitters and receivers for larger-array MIMO systems.

Chapter 6

Summary and Future Research

6.1 Primary Contributions

This dissertation contributes to research efforts to implement a wideband MIMO true array channel sounder, to obtain comprehensive line-of-sight and non-line-of-sight field measurements, to investigate measured MIMO channel capacity, and to analyze and evaluate statistically the Kronecker MIMO model against the measured data. The primary results of the current work are listed below.

6.1.1 Prototyping of Wideband MIMO Testbed

When conducting radio channel measurements in various environments, we must have special equipment and a suitable testbed. Usually, such testing equipment involves huge investment and much engineering design. After three years of hard work on the design and implementation, I have successfully implemented a true-array wideband MIMO channel sounder and conducted channel data collection. There were a considerable number of hardware designs, such as RF circuitry, FPGA, PLL, LO synthesizer, and DAC, as well as software development, such as VHDL for FPGA, gain control, LabVIEW for DAQ, PN probing sequences, and data postprocessing. The final channel sounder operates at 1.8 GHz with a bandwidth of 2.5 MHz. The maximum delay that can be measured is 12μs, and the minimum resolvable delay is 0.4 μs. This channel sounder is well suited for channel measurements in microcell environments. This special tool allows advanced research on the wideband MIMO channel to be conducted[64].

6.1.2 Measurements of Outdoor Wideband Channels

I have collected raw data in various wideband MIMO channels at the J. J. Pickle Research Campus. The raw data reflects the characteristics of real MIMO channels. For example, I have recorded wideband channel data in LOS environments and NLOS environments. These data, which are functions of locations and environments, can be used to evaluate existing channel models and to design future wireless communication systems. With those data, I analyzed the correlation properties of channels in the frequency domain and the space domain. The degree of correlation practically affects the channel capacity [65].

6.2 Summary

The main focus of this dissertation has been the prototyping of a wideband MIMO channel sounder and the use of that prototype in a comprehensive investigation into the measurement of wideband MIMO channels in NLOS environments. A series of measurement campaigns were conducted at the Pickle Research Campus. The measured channel data were statistically analyzed in terms of the RMS delay spread, elements in the matrix channel transfer functions, and the frequency correlation functions.

The measured capacity was represented by a CDF of capacity. When comparing the measured capacity with that of an ideal iid channel realization, we achieved more than 70% of theoretical capacity in the NLOS outdoor channels with a bandwidth of 2.5 MHz for a 4 x 8 MIMO system. It was found that the outage capacity of a wideband channel is higher than the outage capacity of a narrowband channel at low outage rates. This difference is attributed to the increased tightening of the CDF of capacity because of frequency diversity. We evaluated the Kronecker MIMO model using the measured data under different array sizes and channel responses in a typical frequency bin. We found that, with an increase of array size, the model error of the Kronecker model became large, at least from the point of view of CDF of capacity. In other words, the Kronecker model may have some shortcoming in its ability to describe larger array sizes or considerably correlated MIMO systems. The Kronecker model overestimates the correlation of transmitters and receivers of larger-array MIMO systems.

6.3 Future Research

After testing the prototype of the wideband MIMO channel sounder in this dissertation, I suggest further research in the following topics:

- The need to broaden the bandwidth of the testbed by improving the hardware, such as employing fast ADC, DAC, and more memory.

- Wideband mobile MIMO channel measurements and estimation. Many statistics can be obtained, such as time dispersion, frequency dispersion, and spatial diversity.

- Antenna coupling and antenna array imperfections on the MIMO systems, especially the mutual coupling effects on MIMO capacity.

- The power spectral associated with the angle of arrival and angle of departure of the antenna array by using highly directional antennas.

- The possibility of extending the current wideband CDMA to a MIMO-CDMA or a MIMO-OFDM system.

Bibliography

[1] T. S. Rappaport, *Wireless Communications, Principles and Practice.* Englewood Cliffs, NJ: Prentice-Hall, 1996.

[2] J. H. Winters, “On the capacity of radio communication systems with diversity in a Rayleigh fading environment,” *IEEE J. Select Areas Commun.*, vol. SAC-5, pp. 871-878, June 1987.

[3] J. Salz and J. H. Winters, “Effect of fading correlations on adaptive arrays in digital mobile radio,” *IEEE Transactions on Vehicular Technology*, vol. 43, pp. 1049-1057, Nov. 1994.

[4] J. H. Winters, “Smart Antennas for Wireless Systems,” *IEEE Personal Communications Magazine*, vol. 5, pp. 23-27, February 1998.

[5] S. S. Jeng, G. Xu, H. P. Lin and W. J. Vogel, “Experimental studies of spatial signature variation at 900 MHz for smart antenna systems,” *IEEE Trans. on Ant. Prop.*, vol. 46(7), pp. 953-962, July 1998.

[6] K. R. Dandekar, H. Ling, and G. Xu, “Experimental Study of Mutual Coupling Compensation in Smart Antenna Applications,” In *IEEE trans. Wirel. Commun.,* vol. 1, no. 3, pp.480-487, July 2002.

[7] K. R. Dandekar, G. Xu, and H. Ling, "Computational electromagnetic simulation of smart antenna systems in urban microcellular environments," In *IEEE EEE Trans. on Veh. Tec.*, vol. 52, no. 4, pp.733-742, July 2003.

[8] D. A. Gore, R. W. Heath, and A. J. Paulraj, "Transmit selection in spatial multiplexing systems," *IEEE Commun. Lett.,* vol. 6, pp. 491-493, Nov. 2002.

[9] R. W. Heath Jr., S. Sandhu, and A. Paulraj, "Antenna selection for spatial multiplexing systems with linear receivers," *IEEE Commun. Lett.,* vol. 5, pp. 142-144, Apr. 2001.

[10] A. Paulraj, R. Nabar, and D. Gore, *Introduction to Space-Time Wireless Communications.* Cambridge University Press, 2003.

[11] K. Pahlavan and A. H. Levesque, *Wireless Information Networks.* John Wiley and Sons, Inc., 1995.

[12] W. C. Jakes, *Microwave Mobile Communications*, New York: John Wiley and Sons, 1974.

[13] W. C. Y. Lee, *Mobile Communications Design Fundamentals*, New York: John Wiley and Sons, 1993.

[14] A. A. M. Saleh and R. A. Valenzuela, "A statistical model for indoor multipath propagation," *IEEE J. Select Areas Commun.*, vol. SAC-5, pp. 128-137, Feb. 1987.

[15] T. S. Rappaport, S. Y. Seidel, and K. Takamizawa, "Statistical channel impulse response models for factory and open plan building radio commu-

nication system design," *IEEE Trans. Commun.*, vol. 39, pp. 794-807, May 1991.

[16] H. Hashemi, "Impulse response modeling of indoor radio propagation channels," *IEEE J. Select. Areas Commun.,* vol. 11, pp. 967-978, Sept. 1993.

[17] A. J. Goldsmith and L. J. Greenstein, "A measurement-based model for predicting coverage areas of urban microcells," *IEEE J. Select. Areas Commun.* vol. JSAC-11(7), pp. 1013-1023, Sep. 1993.

[18] G. G. Raleigh, S. N. Diggavi, A. F. Naguid, and A. Paulraj, "Characterization of fast fading vector channels for multi-antenna communication systems," *Proc. IEEE Asilomar Conf. on Signals, Systems, and Computers*, (Pacific Grove, CA), vol.2, pp. 853-857, Nov. 1994.

[19] T. S. Rappaport, S. Y. Seidel, and R. Singh, "900 MHz multipath propagation measurements for U.S. digital cellular radio telephone," *IEEE Trans. on Veh. Tec.*, pp.132-139, May 1990.

[20] G. J. Foschini and M. J. Gans, "On limits of wireless communications in a fading environment when using multiple antennas," *Wireless Personal Commun.*, vol. 6, no. 3, pp. 315-335, Mar. 1998.

[21] G. Golden, C. Foschini, R. Valenzuela, and P.Wolniansky, "Detection algorithm and initial laboratory results using V-BLAST space-time communication architecture," *Electron. Lett.*, vol. 35, no. 1, pp. 14-15, Jan. 1999.

[22] C. C. Martin, J. H. Winters, and N. R. Sollenberger, "Multiple-input multiple-output (MIMO) radio channel measurements," *in Proc. IEEE Vehicular Technol. Conf.* (Fall VTC) Boston, MA, vol. 2, Sept. 2000, pp. 774-779.

[23] G. G. Raleigh and J. M.Cioffi, "Spatio-temporal coding for wireless communication," *IEEE Trans. Commun.*, vol. 46, pp. 357-366, Mar. 1998.

[24] A. F. Molisch, M. Steinbauer, M. Toeltsch, E. Bonek, and R. S. Thoma, "Measurement of the capacity of MIMO systems in frequency-selective channels," in *Proc. IEEE 53rd Veh. Technol. Conf.* Rhodes, Greece, vol. 1, May 6-9, 2001, pp. 204-208.

[25] A. F. Molisch, M. Steinbauer, M. Toeltsch, E. Bonek, and R. S. Thoma, "Capacity of MIMO systems based on measured wireless channels," *IEEE J. Select Areas Commun.*, vol. 20, pp. 561-569, Apr. 2002.

[26] K. Yu, M. Bengtsson, B. Ottersten, D. McNamara, P. Karlsson, and M. Beach, "Modeling of wide-band MIMO radio channels based on NLOS indoor measurements," *IEEE Trans. Vehicular Technology*, vol. 53, no.3, pp.655–665, 2004.

[27] D. Gesbert, H. Bolcskei, D.A. Gore, and A.J. Paulraj, "Outdoor MIMO wireless channels: models and performance prediction," *IEEE Trans. Commun.*, vol.50, no.12, pp.1926–1934, 2002.

[28] J. P. Kermoal, L. Schumacher, F. Frederiksen, and P. E. Mogensen, "Polarization diversity in MIMO radio channels: Experimental validation of a

stochastic model and performance assessment," *in Proc. IEEE 54th Veh. Technol. Conf.* Atlantic City, NJ, vol. 1, Oct. 7-11, 2001, pp. 22-26.

[29] S. M. Alamouti, "A simple transmit diversity technique for wireless communications," *IEEE J. Select. Areas Commun.*, vol. 16, pp. 1451-1458, Oct. 1998.

[30] T. Svantesson, "Correlation and channel capacity of MIMO systems employing multimode antennas," *IEEE Trans. Veh. Technol.,* vol. 51, pp. 1304-1312, Nov. 2002.

[31] T. Svantesson, M. A. Jensen, and J. W. Wallace, "Analysis of electromagnetic field polarizations in multi-antenna systems," *IEEE Trans. Wireless Commun.,* vol. 3, Mar. 2004.

[32] D. Gesbert, M. Shafi, D. Shiu, P. J. Smith, and A. Naguib, "From theory to practice: An overview of MIMO space-time coded wireless systems," *IEEE J. Selected Areas in Commun.,* vol.21, no.3, pp.281–302, 2003.

[33] M. A. Jensen and J.W. Wallace, "A review of antennas and propagation for MIMO wireless communications," *IEEE Trans. Antenna and Propagation* , vol. 52, no. 11, pp.2810–2824, 2004.

[34] P. W. Wolniansky, G. J. Foschini, G. D. Golden, and R. A. Valenzuela, "V-BLAST: An architecture for realizing very high data rates over the rich-scattering wireless channel," in *Proc. URSI ISSSE'98* Pisa, Italy, Sept.-Oct. 29-2, 1998, pp. 295-300.

[35] G. German, Q. Spencer, A. Swindlehurst, and R. A. Valenzuela, "Wireless indoor channel modeling: Statistical agreement of ray tracing simula-

tions and channel sounding measurements," in *IEEE Intl. Conf. Acoustics, Speech, Signal Processing* (ICASSP 2001) Salt Lake City, UT, vol. 4, May 2001, pp. 778-781.

[36] G. Athanasiadou, A. Nix, and J. McGeehan, "A microcellular ray-tracing propagation model and evaluation of its narrow-band and wide-band predictions," *IEEE J. Select. Areas Commun.*, vol. 18, pp. 322-335, Mar. 2000.

[37] J. W. Wallace, M. A. Jensen, A. L. Swindlehurst, and B. D. Jeefs, "Experimental characterization of the MIMO wireless channel: data acquisition and analysis," *IEEE Trans. Wirel. Commun.*, 2003, 2, pp.335-343.

[38] D. P. McNamara, M. A. Beach, P. N. Fletcher, and P. Karlsson, "Capacity variation of indoor multiple-input multiple-output channels," *Electron. Lett.*, vol. 36, pp. 2037-2038, Nov. 2000.

[39] J. P. Kermoal, P. E. Mogensen, S. H. Jensen, J. B. Andersen, F. Frederiksen, T. B. Sorensen, and K. I. Pedersen, "Experimental investigation of multipath richness for multi-element transmit and receive antenna arrays," in *Proc. IEEE Vehicular Technol. Conf.* (Spring VTC 2000), Tokyo, Japan, vol. 3, May 2000, pp. 2004-2008.

[40] M. Herdin, H. Ozcelik, H. Hofstetter, and E. Bonek, "Variation of measured indoor MIMO capacity with receive direction and position at 5.2 GHz," *Electron. Lett.*, vol. 38, pp. 1283-1285, Oct. 2002.

[41] K. Yu, M. Bengtsson, B. Ottersten, D. McNamara, P. Karlsson, and M. Beach, "A wideband statistical model for NLOS indoor MIMO channels,"

in*Proc. IEEE 55th Veh. Technol. Conf.* Birmingham, AL, vol. 1, May 6-9, 2002, pp. 370-374.

[42] D. Chizhik, J. Ling, P. Wolniansky, R.Valenzuela,N. Costa, and K. Huber, “Multiple-input-multiple-output measurements and modeling in Manhattan,” *IEEE Trans. on Selected Communications*, vol. 21, no. 3, pp. 321–331, April 2003.

[43] K. Yu, M. Bengtsson, B. Ottersten, D. McNamara, P. Karlsson, and M. Beach, “Second order statistics of NLOS indoor channels based on 5.2 GHz measurements,” in *Proc. IEEE Global Telecommunications conf.*, vol.1, pp.156–160, 2001.

[44] M. D. Batariere, T. K. Blankenship, J. F. Kepler, T. P. Krauss, I. Lisica, S. Mukthavaram, J. W. Porter, T. A. Thomas, and F. W. Vook, “Wideband MIMO mobile impulse response measurements at 3.7 GHz,” in *Proc. IEEE 55th Veh. Technol. Conf.* Birmingham, AL, vol. 1, May 6-9, 2002, pp. 26-30.

[45] V. Erceg, P. Soma, D. S. Baum, and A. J. Paulraj, “Capacity obtained from multiple-input multiple-output channel measurements in fixed wireless environments at 2.5 GHz,” in *Proc. IEEE Int. Conf. Commun.* New York, NY, vol. 1, Apr.-May 28-2, 2002, pp. 396-400.

[46] P. Soma, D. S. Baum, V. Erceg, R. Krishnamoorthy, and A. J. Paulraj, “Analysis and modeling of multiple-input multiple-output (MIMO) radio channel based on outdoor measurements conducted at 2.5 GHz for fixed BWA applications,” in *Proc. IEEE Int. Conf. Commun.* New York, vol. 1, Apr.-May 28-2, 2002, pp. 272-276.

[47] A. Gupta, A. Forenza, R. W. Heath, "Rapid MIMO-OFDM software defined radio system prototyping," in *IEEE Workshop on Signal Processing Systems*, (SIPS 2004), 2004, pp. 182-187.

[48] M. Batariere, J. Kepler, T. Krauss, S. Mukthanvaram, J. Porter, and F. Vook J. Kepler, T. Krauss, and S. Mukthanvaram, "Delay spread measurements on a wideband MIMO channel at 3.7 GHz," *IEEE VTC-2002/Fall*, vol. 4 pp. 2498–2502, 2002.

[49] A. Adjoudani, E. C. Beck, A. P. Burg, G. M. Djuknic, T. G. Gvoth, D. Haessig, S. Manji, M. A. Milbrodt, M. Rupp, D. Samardzija, A. B. Siegel, T. Sizer, C. Tran, S. Walker, S. A. Wilkus, and P. W. Wolniansky, "Prototype experience for MIMO BLAST over third-generation wireless system," *IEEE J. Select. Areas Commun.* vol. 21, no.3 pp.440-451 , April 2003.

[50] M. J. Gans, N. Amitay, Y. S. Yeh, H. Xu, T. C. Damen, R. A. Valenzuela, T. Sizer, R. Storz, D. Taylor, W. M. MacDonald, C. Tran, and A. Adamiecki, "Outdoor BLAST measurement system at 2.44 GHz: calibration and initial results," *IEEE J. Select. Areas Commun.* vol. 20, no.3 pp.570-583 , April 2002.

[51] N. Papadakis, A. Hatziefremidis, A. Tserolas, and P. Constantinou, "Wideband propagation measurement and modeling in indoor environment," *Interational Journal of Wireless Information Networks* vol. 4, No.2, pp. 101-111, 1997.

[52] M. A. Do and Sumei Sun, "Statistical modeling of broadband wireless

LAN channels at 18 GHz using directive antennas," *Interational Journal of Wireless Information Networks* vol. 4, No.1, pp. 21-30, 1997.

[53] D.-S. Shiu, G. J. Foschini, M. J. Gans, and J. M. Kahn, "Fading correlation and its effect on the capacity of multielment antenna systems," *IEEE Trans. on Commun.*, vol. 48, No.3, pp. 502–513, 2000.

[54] D. Chizhik, F. Rashid-Farrokhi, J. Ling, and A. Lozano, "Effect of antenna separation on the capacity of BLAST in correlated channels," *IEEE Commun. Lett.*, vol. 4, pp. 337-339, Nov. 2000.

[55] C.-N. Chuah, D. N. C. Tse, J. M. Kahn, and R. A. Valenzuela, "Capacity scaling in MIMO wireless systems under correlated fading," *IEEE Trans. Inf. Theory*, vol. 48, pp. 637-650, Mar. 2002.

[56] J. W. Wallace and M. A. Jensen, "Statistical characteristics of measured MIMO wireless channel data and comparison to conventional models," in *Proc. IEEE 54th Veh. Technol. Conf.* Atlantic City, NJ, vol. 2, Oct. 7-11, 2001, pp. 1078-1082.

[57] D. P. Palomar, J. R. Fonollosa, and M. A. Lagunas, "Capacity results of spatially correlated frequency-selective MIMO channels in UMTS," in *Proc. IEEE VTC'01*, vol. 2, 2001, pp. 553-557.

[58] A. Pal, C. M. Tan, and M. A. Beach "Comparison of MIMO channels from multipath parameter extraction and direct channel measurements," *IEEE International Symposium on Personal, Indoor and Mobile Radio Communications*, 5-8 Sept. 2004 Volume 3, pp.1574–1578, 2004.

[59] C. Xiao, J. Wu, S.-Y. Leong, Y. R. Zheng, and K. B. Letaief, "A discrete-time model for spatio-temporally correlated mimo wssus multipath channels," in *Proc. IEEE Wireless Comm. and Networking Conf.* New Orleans, LA, vol. 1, Mar. 16-20, 2003, pp. 354-358.

[60] A. M. Sayeed, " Deconstructing multi-antenna fading channels," *IEEE Trans. Signal Processing*, vol. 50, pp. 2563-2579, Oct. 2002.

[61] J. Kermoal, L. Schumacher, K. Pedersen,P. Mogensen, F. Frederoksen, "A stochastic MIMO radio channel model with experimental validation," *IEEE Trans. on Selected Communications*, vol. 20, no. 6, pp. 1214–1226, Aug. 2002.

[62] G. H. Golub and C. F. Van Loan, *Matrix Computations.* The Johns Hopkins University Press, London, 3rd edition, 1996.

[63] H. Ozcelik, M. Herdin, W. Weichselberger, J. Wallace, and E. Bonek, "Deficiencies of the Kronecker MIMO radio channel model," *Electron. Lett.*, vol. 39, pp. 1209-1210, Aug. 2003.

[64] Y. Yang, G. Xu, and H. Ling, " An Experimental Investigation of Wideband MIMO Channel Characteristics Based on Outdoor Non-LOS Measurements at 1.8 GHz," accepted under revisions to *IEEE Trans. Antenna Propagat., Special Issue on Wireless Communications,* March 2006.

[65] Y. Yang, G. Xu, and H. Ling, "Wideband MIMO Measurements of Outdoor Non LOS Channels," *Microwave Opt. Technol. Lett.,* Vol.48, pp.216-218, Feb. 2006.

Vita

Yaoqing Yang is from Beijing, China. He received his Bachelor of Science in Electrical Engineering from Northern Jiantong University in July 1983, and he received a Master of Science in Electrical Engineering from Beijing Broadcast Institute in December 1986. He served as a teacher and engineer at the Beijing Broadcast Institute between December 1996 and July 1997. In August 1997 he entered The University of Texas at Austin (UT) as an exchange visitor and worked on a semiconductor project sponsored by the National Science Foundation. In spring 1999, he began his Ph.D program at UT, and at the same time he continued to contribute to the semiconductor project until its completion. From 2000 to 2003, he worked on the Advanced Research Program (ARP) project for smart antenna measurements. Later, he developed a 4 x 8 wideband MIMO channel sounder that incorporated spread spectrum technology. In May 2006, he received his Ph.D in the area of wireless communication from the Department of Electrical and Computer Engineering of The University of Texas at Austin.

Permanent Address: Room 1004, Bldg. 13, Ding Fu Zhuang Dongji,
Beijing, China 100024

This dissertation was typeset with LaTeX 2_ε by the author.